1994

Thermocapillary convection and solidification in rectrangular cavities

Xun L. Chen
Lehigh University

AUTHOR:

Chen, Xun L.

TITLE:

Thermocapillary Convection and Solidification in Rectangular Cavities

DATE: May 29, 1994

THERMOCAPILLARY CONVECTION AND SOLIDIFICATION IN RECTANGULAR CAVITIES

by

Xun L. Chen

A Thesis

Presented to the Graduate and Research Committee

of Lehigh University

in Candidacy for the Degree of

Master of Science

in Mechanical Engineering

Lehigh University

May, 1994

This thesis is accepted and approved in partial fulfillment of the requirements for the degree of Master of Science in Mechanical Engineering.

May 9, 1994

Date

Thesis Advisor

Chairman of Mechanical Engineering and Mechanics

Acknowledgements

I am extremely grateful to my parents and my grandmother for their love and support throughout my adventures in academia.

I would also like to thank Dr. A. Liakopoulos for his encouragement, guidance, and support during my graduate study at Lehigh.

Table of Contents

Abstract

The purpose of this thesis is to establish the feasibility of simulating accurately processes occurring during crystal growth from the melt using spectral element methods. Instead of trying to directly simulate the complex configurations encountered in practice, we have chosen to investigate four idealized problems that address the basic modeling issues to be resolved: thermocapillary convection, natural convection, and propagation of solidification fronts. All simulations performed are time accurate. If a steady (time-independent) solution exists it is found as the steady-state solutions of the appropriate initial boundary value problem after all transients die out, i.e., in the limit $t \to \infty$.

The first part of this thesis investigates the characteristics of thermocapillary convection in a two dimensional shallow cavity of aspect ratio 0.25, with differentially heated side walls, Re=7200, Pr=0.015, Bi=0, Bo=0, and Ca=0.01. Patterns of free surface deformation and streamlines during the transient system response are studied. The second part of the thesis takes a module out of a long, shallow cavity and investigates the characteristics of the thermocapillary flow within this computational domain. For this problem, $100 \leq Re \leq 50{,}000$, Pr=0.01, Ca=0.01, and Bo=0. Free surface characteristics, i.e., displacement, speed, and pressure variation, along with isotherm, streamline, and voticity patterns within the computational domain are studied in detail. The solutions exhibit maximum symmetry consistent with the boundary conditions. No temporal instabilities have been observed in the range of parameters

considered. For large values of Reynolds number, vorticity is uniform within regions of closed streamlines in accordance with the Prandtl-Batchelor theorem.

The third part of the thesis analyzes a solidification process in a closed rectangular cavity in the presence of strong buoyancy effects. Numerical calculations are carried out for $3.55\text{x}10^{-3} \leq Gr \leq 106500$, Pr=1, and Ja=0.64. Our concentration in this part of the research is in the observation of the solid/liquid interphase propagation, deformation, and the melt back process observed at high values of Grashof number. The last part of this thesis investigates the characteristics of thermocapillary convection with phase change in a two dimensional square cavity. The Reynolds and Prandtl numbers in this case are $1\text{x}10^3$ and 1, correspondingly, Ja=0.014, and Gr=0. The approach looks very promising, but requires a new numerical algorithm, allowing larger values of Δt, to be developed before attempting to simulate realistic configurations of crystal growth processes from the melt. Alternatively, a scaling of the problem can be devised in order to rigorously simplify the mathematical model.

I. INTRODUCTION

Today's semiconductor manufacturing technology requires high quality single crystal materials. Silicon, germanium, and gallium arsenide are used for integrated circuit fabrication. These crystals are commonly grown by crystallization from the melt. The two most critical issues in crystal growth are the control of the temperature within the crystal and the shape and position of the solid/liquid interface, Young *et al.* (1992).

In addition to natural convection, i.e., buoyancy driven flow, thermocapillary convection plays an important role in the process. Thermocapillary convection is the fluid motion induced by variations of surface tension on a liquid/gas interface resulting from a nonuniform temperature distribution. This type of convection plays an important role in many technological and engineering-science applications, welding and crystal growth from the melt being the most important. Common methods used to grow single crystals are the Czochralski, Bridgman, and the floating zone method. The Czochralski method (Fig. 1.1a) involves dipping a crystalline seed, which is rotating in a chuck, into a crucible of melt. The temperature above the melt is controlled so that crystalline material grows from the seed as it is pulled from the melt. Growing crystals using a Bridgman furnace (Fig. 1.1b) involves moving a multi-zone furnace over an ampoule that contains the source material. The furnace, which has a hot zone (temperature higher than the melting temperature) and a cold zone (temperature lower than the melting temperature) separated by an adiabatic zone, passes over the ampoule, and material solidifies

into a crystalline state starting from the seed which is located at one end of the ampoule. The temperatures of the hot and cold zone are specified such that the solid/liquid interface is positioned within the adiabatic zone. The adiabatic zone smooths out temperature gradients that occur across the interface and aids in controlling the shape of the interface. Unlike the Bridgman technique, which the melt is contained in a crucible and the melt-crystal interface contacts with the crucible, the floating zone (Fig. 1.1c) technique does not require a container and is more likely to produce crystals of the highest quality in microgravity environment.

In this thesis we consider fluid flow and heat transfer in four idealized configurations with thermal conditions that cause thermocapillary convection, natural convection and solidification/melting processes. It is hoped that experience gained from this work will lead to more realistic models of various crystal growth processes used in practice. A list of symbols that are used in this thesis is shown in Table 1.

Nomenclature

A	aspect ratio
α	thermal diffusivity
Bi	Biot number, $Bi = \frac{hl}{k}$
β	thermal expansion coefficient
Bo	static Bond number, $Bo = \frac{\rho_0 g L^2}{\sigma_0}$
Ca	capillary number, $Ca = \frac{1}{S}$
c_p	specific heat
Gr	Grashof number, $Gr = \frac{\beta g L^3 \Delta T}{\nu^2}$
γ	temperature coefficient of surface tension
H	cavity height
h	latent heat of fusion
Ja	Jacob number, $Ja = \frac{c\Delta T}{h}$
k	thermal conductivity
L	cavity length
Ma	Marangoni number, $Ma = Pr\ Re = \frac{L\gamma\Delta T}{\mu\alpha}$
μ	dynamic viscosity
$\hat{\boldsymbol{n}}$	normal direction
Nu	Nusselt number
ν	kinematic viscosity
p	pressure
Pe	Peclet number, $Pe = \frac{UL}{\alpha}$
Pr	Prandtl number, $Pr = \frac{\nu}{\alpha}$
$q(x)$	heat flux

R	radius of curvature
Ra	Rayleigh number
ρ	density
Re	Reynolds number, $Re = \frac{UL}{\nu}$
S	surface tension number, $S = \frac{\sigma_0}{\gamma \Delta T}$
$\hat{s}$	tangential direction
σ	surface tension
T	temperature
τ	shear stress
θ	dimensionless temperature
U	vector velocity, $U = u\hat{i} + v\hat{j}$
u	velocity component in x-direction
v	velocity component in y-direction

Superscripts:

$*$	dimensionless quantity
$'$	first derivative
$''$	second derivative

Subscripts:

ref	reference quantity
f	conditions at freezing/melting front

Table 1 Nomenclature

(a) Overview of Numerical Studies

i) Studies on Thermocapillary Effects

Many numerical simulations have been done on thermocapillary flows in two-dimensional cavities. Damian Rivas (1990) studied the steady thermocapillary flows of low-Prandtl-number fluids in shallow ($A = 0.2$) rectangular enclosures under an imposed-heat-flux configuration in the absence of gravitational forces. He considered low-Prandtl-number fluids, i.e., fluids whose ability to diffuse heat is much greater than their ability to diffuse vorticity. In this case the formulation is simplified considerably since the energy equation is reduced to a simple conduction equation, where by the temperature field becomes decoupled from the flow field. Rivas solved the Navier-Stokes equations numerically for Reynolds numbers up to 10^4. In his numerical simulation, the free surface was assumed flat. This assumption is true for small capillary numbers (Rivas used 0.01). His study found the existence of a boundary layer along the free surface and the existence of a strong vortex close to the vertical wall for flows with Reynolds numbers greater than 10^3. The size of the vortex was practically independent of the Reynolds number.

Chen, Sheu and Jwu (1990) performed a study on thermocapillary convection in a rectangular cavity with top free surface subjected to inhomogeneous heating. The Navier-Stokes equations and the energy equation were solved by a finite-difference method with a boundary-fitted curvilinear coordinate system. The buoyancy effect was ignored in their research. Their geometries had two aspect ratios: 0.2 and 1. The Reynolds numbers in their study were in the range from 1 to 5000. One part of their study was to examine

the effect of the capillary number on the flow field, the temperature field, and the surface deflection. While holding $A = 0.2$, $Bi = 1$, $Re = 5$, and $Ma = 1$, computations were performed by varying Ca from 0.04 to 0.32. Results showed that the surface deflection increased for high Ca. The effect of the Reynolds number on the solutions was also studied. Plots of the streamline and isotherms for $A = 1$, $Ca = 0.16$, $Pr = 0.2$, and $Bi = 1$ with different values of Re showed that with $Re < 1500$, the magnitude of surface deflection increased with increasing Re, while with $Re > 1500$, the magnitude of surface deflection decreased with increasing Re. Finally, the effect of the Prandtl number was presented. The results indicated that when $Pr < 1$, the convective effect on the velocity field was more important near the cold corner and the isotherm pattern reflects the dominance of conduction. For $Pr > 1$, the isotherm pattern showed the transition from a conduction-dominated region to a convection-dominated region. The convection became more significant at the hot corner, and the streamline and isotherm patterns were modified dramatically near the hot corner.

Sen and Davis (1982) studied the steady thermocapillary flows in a two-dimensional slot with a temperature gradient applied along its free surface. Their work was very close to Chen, Sheu, and Jwu's (1990), with solutions obtained for both fixed lines and fixed angles at the contact between the interface and the solid side walls. Sen and Davis found that an asymptotic theory was valid for $A = \frac{Height}{Length} \to 0$.

There was a two-part study done on high Marangoni number convection in a square cavity. The first part was done by Zebib, Homsy, and Meiburg (1985). In order to assume a flat top free surface, only the case of $Ca \to 0$ was considered.

This part of the study indicated that for Prandtl number other than unity, the largest value of Ma attainable with reasonable accuracy was $5x10^4$. Plots showed that with increasing Re, the surface vorticity at the hot corner first decreased, and then began to increase monotonically with further increase in Re. This was similar to the case when the Prandtl number was equal to unity. The second part of the work was done by Carpenter and Homsy (1990). They found that the character of thermocapillary flow was highly sensitive to the value of the Prandtl number over a range of Marangoni numbers exceeding $1x10^5$ for $1 \leq Pr \leq 50$, the magnitude of the flow showing non-monotonic dependence on the Marangoni number for $Pr \leq 10$. They also dealt with the scaling behavior of thermocapillary flow at large Reynolds numbers. They studied the Prandtl number dependence of the thermocapillary flow and found that the flow was extremely sensitive to this parameter, not only in regard to the magnitude of the flow, as was the case in high Grashof number buoyancy-driven convection, but also with respect to the structure and scaling of the flow. This sensitivity was mainly due to the strong influence of the Prandtl number on the free surface temperature distribution, as this distribution was independent of the Reynolds number as $Re \rightarrow \infty$.

ii) Studies on Combined Buoyant and Thermocapillary Effects

A number of studies were conducted on the combined effects of buoyant and thermocapillary convections. Ramaswamy and Jue (1992) used a semi-implicit scheme based on the operator-splitting finite-element method to show the interaction between the buoyancy and the surface tension forces. The cases

investigated here include $Ra = 1, 10^4$; $|Ma| < 10^4$; $Pr = 5, 0.71$; and $A = 2, 1, 0.5$. They found that the Marangoni number strongly affected the flow field as well as the heat transfer phenomena, and low aspect ratio and Prandtl number enhanced the thermocapillary flow development. Like Chen, Sheu, and Jue (1990), Ramaswamy and Jue also studied the effects of the Marangoni number, the Prandtl number, and the aspect ratio. In illustrating the Marangoni number effects, positive Ma was used for augmenting surface tension and negative for counteracting surface tension. Plots of streamlines showed that counteracting surface tension reversed the horizontal velocity on the free surface, thus resulting in a dramatically different flow pattern. With surface tension augmenting buoyancy, the local Nusselt number at the top of the cold wall displayed a large value, owing to the isotherm compaction. In the study of the Prandtl number, Ramaswamy and Jue showed that for small Pr, the surface tension effect is reduced. This agreed with the results from Chen, Sheu, and Jue (1990). In the augmenting case, the strength is weaker and the isothermal lines are smoother compared with the high Prandtl number results. Similarly, the circulation driven by surface tension was reduced in the counteracting case. The Nusselt number and free-surface velocity also became small because of the low Prandtl number. In addition to Pr, the aspect ratio played another important factor for the flow that they had studied. With small aspect ratio ($A = 0.5$), the distance for buoyancy transfer was twice the distance for surface tension transfer, while with large aspect ratio ($A = 2$), the surface tension effect was confined to the top portion and the remaining portion was dominated by buoyancy-driven flow.

Lai and Chang (1991) also numerically studied the thermocapillary flows in

a two-dimensional cavity with a specified heat flux imposed upon the free surface. The Prandtl numbers in their study ranged from 10^{-2} to 10^{2}; Reynolds numbers varied from 10^{3} to 10^{8}. The aspect ratios involved in their studies varied from 0.1 to 1. While Rivas (1990) ignored the existence of the gravitational effect, Lai and Chang included this effect. Their dynamic Bond number ranged from 10 to 10^{4}. Their result indicated that: (1) The oscillation phenomenon did not exist for such a flow configuration; (2) The buoyancy effect may augment the thermocapillary flow motion; (3) The secondary cellular flow motion near the side walls was possibly induced by an over-cooling of the bottom wall.

Ben Hadid and Roux (1989) performed a similar study as done by Ramaswamy and Jue. Instead of having differentially heated side walls with constant temperatures, Ben Hadid and Roux considered the side walls as perfectly conducting with linear temperature profiles. For their rectangular shaped geometry, $A = 0.04$, and $Pr = 0.015$. With two values of Grashof number, $3\text{x}10^{3}$ and $6\text{x}10^{3}$, the Reynolds number was varied from negative to positive values to show the stability of the combined convection. They found that a critical Grashof number, Gr_c, for the onset of the oscillatory regime substantially decreased with small negative Re, and increased with positive Re. But the thermocapillary forces had again an important stabilizing role for high negative values of Reynolds numbers. For $Re > 0$, the surface velocity progressively became thermocapillary-controlled. For $Re < 0$, with smaller Gr ($Gr = 3\text{x}10^{3}$), two distinguished flows existed. One was generated by buoyancy forces, rising along the hot wall and circulating from cold to hot along the bottom wall. The

second one was thermocapillary-driven, circulating from cold to hot along the upper surface.

Berman and Keller (1988) studied the characteristics of combined buoyancy and thermocapillary flow for liquid metals in a rectangular cavity. Their results showed that, for augmenting buoyancy and surface tension forces, qualitative flow patterns and isotherms were unchanged, but enhanced fluid velocities and heat transfer rates occurred. In contrast, for counteracting buoyancy and surface tension forces, three different flow regimes were identified, with minimum heat transfer rates occurring when buoyancy and surface tension were of equal importance. The aspect ratios used in their study were of 0.5, 1.0, and 2.0.

Buckle and Peric (1992) presented a simulation of such a convection in a square cavity with differentially heated side walls and top free surface. A comparison was made with experimental observations of Metzger and Schwabe (1988). The numerical results agreed well with the experimental ones.

iii) Studies of Combined Effects in Three-Dimensional Domain

While most of the studies were done in a two-dimensional domain, Mundrane and Zebib (1992) performed a study of both two and three-dimensional buoyant thermocapillary convection. Their flow was assumed to be spatially periodic within the cavity, isothermal at other vertical boundaries, and adiabatic at horizontal ones. The Prandtl number, Marangoni number to Grashof number ratio, and geometry were fixed while the Marangoni number was varied over sufficient range to demonstrate a bifurcation from two-dimensional to

three-dimensional flow. Results indicated that the critical Marangoni number was at a value of $Ma_c = 1.95\text{x}10^5$. Their work was a numerical duplicate of the similar experiment. And the two methods agreed with each other well.

iv) Studies of Surface Contamination Effects

Chen and Kuan (1991) studied the influence of surface contamination over the thermocapillary convection in a rectangular cavity. Their results showed that the thermocapillary convection could be stabilized by the addition of an insoluble surfactant. Furthermore, as the concentration of the surfactant increases, oscillatory instability caused by this surfactant may occur when the slope of the surface tension becomes negative. The influences of the elasticity (E) and Peclet (Pe) numbers on the surface deformation were studied. They found that the amount of surface deflection decreased as E and Pe increased.

v) Studies on Solid/Liquid Phase Change Effects

Solid-liquid phase change is a basic heat transfer phenomenon which is very important in a variety of industrial applications. To date, considerable efforts have been dedicated to obtain the solution of freezing or melting problems both in the absence of liquid phase convection and in situations where natural convection in the melt significantly affects freezing and melting.

1) Phase Change with Natural Convection Present in the Liquid Phase

Gadgil and Gobin (1984) performed an analysis of two-dimensional melting in rectangular enclosures with the presence of convection. Their numerical prediction of the solid-liquid boundary at high Ra numbers ($10^6 < Ra < 10^{10}$) was

in good agreement with the experimental result. The numerically predicted speed of propagation of the melting front was 37 percent larger than that observed experimentally. This difference appeared to be acceptable, according to the authors, in the light to the significant side wall heat losses reported in the experiment.

2) Phase Change with Thermocapillary Convection in the Liquid Phase

Bergman and Webb (1989) presented some analytical results for the melting of a pure metal from an isothermal vertical wall. Their investigation focused on the influence of surface tension on the flow and heat transfer in the liquid phase as well as the resultant shape and motion of the solid-liquid interface. Numerical predictions revealed a complex interaction between buoyancy forces in the melt and the Marangoni effects at the melt free surface. Their results showed that the surface tension-driven convection caused an isotherm compaction near the top of, and adjacent to the melting front. Hence the influence of Marangoni convection was felt strongly in the time evolution of shape and motion of the solid-liquid interface.

3) Phase Change with Combined Natural and Thermocapillary Convection

Shyy and Chen (1990) studied the interaction of thermocapillary and natural convection flows during solidification with normal and reduced gravities. They found that in general, as Marangoni number increased, the phase interface was of stronger curvature due to enhanced convection, and the temperature as well as velocity gradients along the free surface also increased. They used a wide

range of Ma, up to 8400, in a square calculation domain. Two Prandtl numbers, 10 and 1.49×10^{-2} were considered. Under normal gravity, the Rayleigh number was assigned to 4.6×10^4 for all cases of counteracting mode, and the multiple-cell convection pattern existed with a wide variation of Marangoni and Prandtl numbers. For the augmenting mode, Ra was either 4.6×10^4 or 4.6×10^6, and convection field exhibited thin-layer, multiple-cell, or single-cell patterns. For the cases under microgravity, Ra was taken as 4.6 for all cases, and convection was always of a single-cell pattern while the thickness of mushy zone changes noticeably with the direction for Marangoni convection.

Liu, Voth, and Bergman (1993) considered melting and solidification of pure material, during which liquid convection was driven by buoyancy, or a combination of buoyancy and surface tension forces. The numerical model showed that thermocapillary effects was of primary influence upon local melting rates in both relatively high and low Pr materials, and it had a significant impact upon overall solidification. In low Pr material, overall solidification rates were affected by thermocapillary convection more than overall melting rates. Thermocapillary convection was shown to have a significant influence upon phase change, regardless of the value of the dynamic Bond number, according to the authors. Their results were compared with experimental results, and showed good agreement.

Young, McDonald, Palazoglu, and Ford (1992) used the boundary element method (BEM) to obtain the temperature field and the shape and position of the solid/liquid interface for bulk crystalline growth in a 3-zone Bridgman furnace. The BEM method transformed a PDE , describing the behavior of the dependent

variable inside a domain and along its boundary, into an integral equation which only required information along the boundary. Their results indicated that for hot and cold zone temperatures that were symmetric about the melting temperature, the interface was planar and positioned at the center of the adiabatic zone when the thermal conductivities of each phase were identical. They showed the effect of the Peclet number on the position and shape of the solid-liquid interface. For fixed melting temperature and Biot number, an increase in Pe moved the interface position toward the cold zone, and made the shape of the interface more parabolic. According to the authors, the Biot number also played an important role in Bridgman crystal growth. It influenced the sensitivity of the interface shape and position with variations in the Peclet number; smaller Biot numbers resulted in an interface that was more sensitive to changes in Peclet number. The last part of their study was on the effect of adiabatic zone length. Results showed that increasing the adiabatic zone length reduced the curvature of the interface but did not affect the relative position of the interface within the adiabatic zone.

vi) Summary on Numerical Studies

Most of the research work done on thermocapillary convection is done numerically, while fewer is done experimentally. Numerical computation is much easier and faster nowadays with the aid of modern computers. Some researchers also performed experimental procedures to make sure that their numerical observations were correct. In our work, which is purely numerical, we begin our study on cases with simple thermocapillary effects and a case on simple

solidification; then we combine the two driving forces together to observe a more complicated thermocapillary effect with the presence of solidification.

(b) Overview of Experimental Studies

i) Studies on Thermocapillary Effects

While most of the research was done numerically, only a few studies were done experimentally. Schwabe, Moller, Schneider, and Scharmann (1992) experimentally studied the instabilities of shallow dynamic thermocapillary liquid layers. Their fluid, ethanol (C_2H_5OH), had a Prandtl number of 17. Because of the small depth, buoyancy effects were neglected. A single-roll state was observed for small Marangoni numbers ($Ma < 6.2\text{x}10^3$). Increase of Ma ($Ma > 6.9\text{x}10^3$) lead to a multiroll state with the roll diameter depended on the depth d of the liquid. From the single-roll state to the multiroll state, the flow went from steady (single-roll state) to oscillatory (multiroll state), and eventually, became more complicated periodic or chaotic flow.

Cardin, Nataf, and Dewost (1991) studied the thermal coupling in layered convection (silicone oil over glycerol, in particular) both experimentally and analytically. In the experimental part of the research, they studied the dynamical role of the interface, by inducing roll-like motions in one of the liquid layers, using a system of two inversely rotating cylinders. Streamlines and velocities on both sides of the interface were then measured, by observing suspended aluminum particles. The results strongly depended upon the sense of rotation of the cylinders (convergence, i.e., rotating in the same sense, or divergence, i.e., rotating in the opposite sense), and upon the amplitude of the

imposed velocity. A numerical analysis was carried out and the results agreed well with the experimental ones.

Camel, Tison, and Favier (1986) developed an experimental method to measure the velocities of inert particles at the surface of thin liquid metal (liquid Sn) layers of Marangoni flows. A plot of velocity vs. Reynolds number showed that for $Re < 10^3$, a linear relationship was obtained, which was consistent with the viscous (theoretical) flow regime. For $Re > 10^3$, experimental points were systematically lower than the theoretical curve. The main reason here was that the contribution of the underlying buoyancy driven flow was not negligible in this range, but should increase the surface velocity rather than decrease it. Thus the observed departure from the theoretical curve might be due to the occurrence of a Marangoni boundary layer flow.

ii) Studies on Combined Thermocapillary and Buoyant Effects

Metzger and Schwabe (1988) performed an experiment which many researchers have done numerically. Their geometry was a square cavity with free surface heated from the side. Buoyancy and thermocapillarity were varied by generating the temperature gradient along the free surface independently from that of the bulk liquid (ethanol with $Pr = 17$ at $20^{\circ}C$). Their experimental results were compared with Zebib, Homsy, and Meiburg's (1985) numerical results. The authors found that even at high Grashof numbers the surface tension driven convection was the dominant effect near the surface. Large Grashof numbers caused by increasing the cavity depth could not influence the surface roll significantly, but both positive and negative Grashof numbers

increased the velocities in the surface vortex. Their experiment was designed to show the importance and strength of surface tension driven flow in thermal convection and they found that the Marangoni effect was significant in the investigated cavity with dimensions of a few centimeters. They also mentioned that the flow remained stationary for small Marangoni numbers, but at high Marangoni numbers time dependent flow was observed.

(c) Problem Definition

In this thesis, four different cases of thermocapillary convection with or without phase change will be studied. The first case is of a shallow cavity with adiabatic top free surface and differentially heated side walls. The second case is of a shallow cavity with top free surface, imposed temperature temperature distribution at the free surface, and periodic conditions over the vertical boundaries. The bottom wall for the first case is insulated, while for the second is at a constant temperature. The third case that we are going to analyze is a solidification problem in a closed shallow cavity. In this case, the liquid phase is in motion due to pure natural convection, with no capillary effects. The side walls in this problem are differentially heated, while the top and bottom walls are both insulated. The last case combines the first and the third case. The geometry is a square cavity such that the solidification process starts from the right vertical wall. The top free surface and the bottom wall are both insulated. The last problem is a generalization of the thermocapillary flow without phase change studied by G. Brown in his M.S. thesis.

(d) Thesis Organization

In Chapter II we present the general mathematical model developed for two-dimensional problems involving natural convection, thermocapillary convection and solidification/melting processes. In this chapter, governing equations, boundary conditions, and initial conditions will be presented in dimensional form. In Chapter III we present the method of solution and the spectral and ALE (arbitrary-Lagrangian-Eulerian) techniques. Finally, the results of the numerical simulations are presented in non-dimensional form in Chapter IV, and conclusions will be drawn in Chapter V.

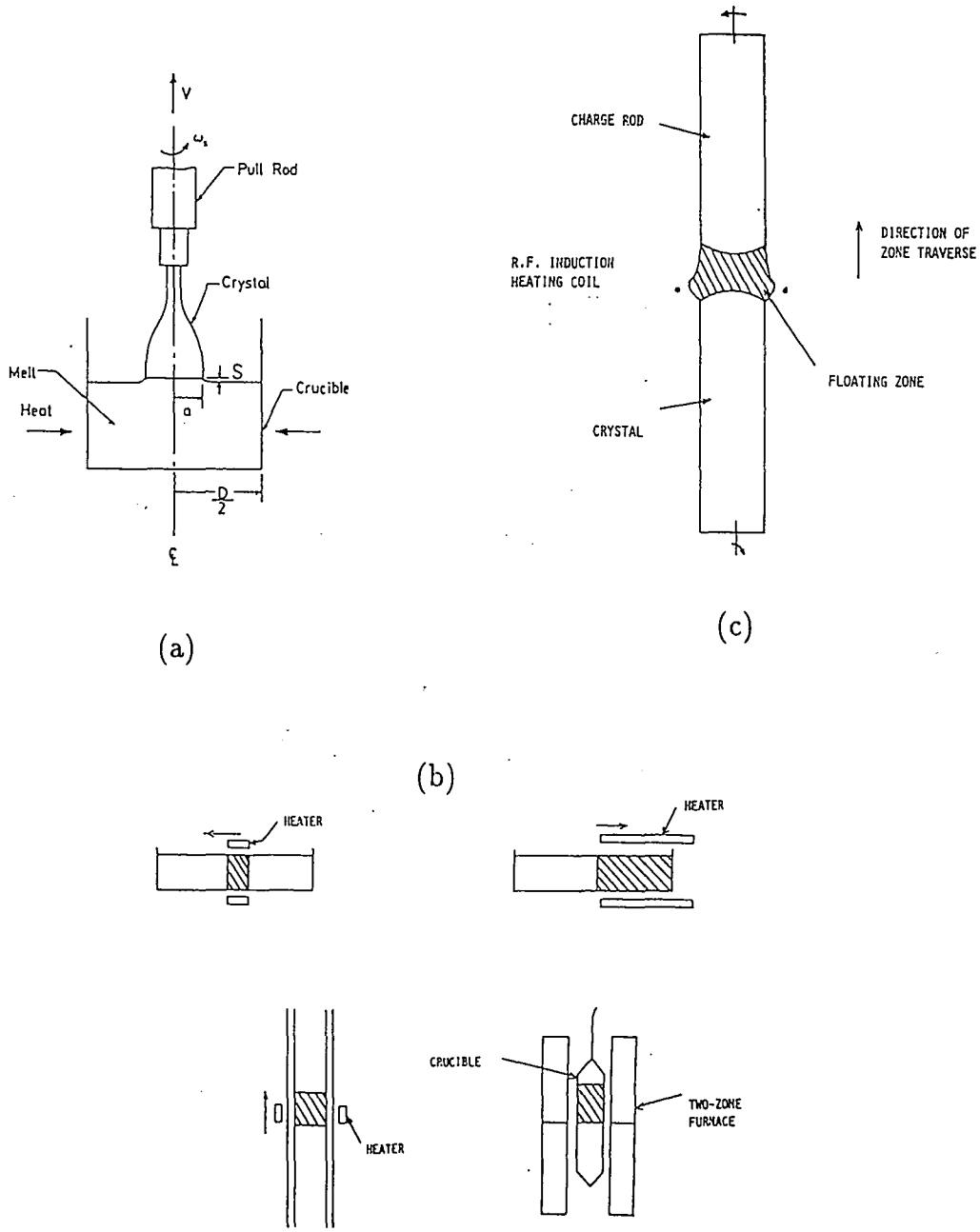

Fig. 1.1 Crystal growth methods.

(a) Czochralski method, (b) Bridgman method, (c) Floating zone method.

II. THE MATHEMATICAL MODEL

In this chapter, we will present the equations that describe fluid flow and heat transfer under the combination of any two or all of the following effects: thermocapillary convection, natural convection, and freezing/melting.

(a) The Governing Equations

The governing equations for the general system considered in this thesis express mathematically the physical principles of conservation of mass, momentum, and energy. For 2-D problems in rectangular coordinates the velocity field is defined as $U = u\hat{i} + v\hat{j}$. Then, conservation of mass for incompressible flows can be expressed by

$$\frac{\partial u}{\partial x} + \frac{\partial v}{\partial y} = 0. \tag{2.1}$$

If we let $T(x,y,t) = T_0 + T_1(x,y,t)$, $p(x,y,t) = p_0(y) + p_1(x,y,t)$, and $\rho(x,y,t) = \rho_0 + \rho_1(x,y,t)$, where T_0 and ρ_0 are constants, and $p_0(y)$ denotes the pressure variation with elevation in the motionless fluid, conservation of momentum in both x and y directions can be expressed by the Navier-Stokes equations in the form

$$\rho_0 \left(\frac{\partial u}{\partial t} + u\frac{\partial u}{\partial x} + v\frac{\partial u}{\partial y}\right) = - \frac{\partial p_1}{\partial x} + \mu \left(\frac{\partial^2 u}{\partial x^2} + \frac{\partial^2 u}{\partial y^2}\right), \tag{2.2}$$

$$\rho_0 \left(\frac{\partial v}{\partial t} + u\frac{\partial v}{\partial x} + v\frac{\partial v}{\partial y}\right) = - \frac{\partial p_1}{\partial y} + \mu \left(\frac{\partial^2 v}{\partial x^2} + \frac{\partial^2 v}{\partial y^2}\right) + \rho_0 \beta g\, T_1. \tag{2.3}$$

In equation (2.3), it is assumed that the acceleration of gravity vector is in the $-\hat{j}$ direction and that the Boussinesq approximation holds. In the above, μ denotes

the dynamic viscosity, β is the coefficient of volumetric expansion, and g is the gravitational constant. Finally, the equation of conservation of energy can be expressed by

$$\rho_0 c_p \left(\frac{\partial T_1}{\partial t} + u\frac{\partial T_1}{\partial x} + v\frac{\partial T_1}{\partial y}\right) = k \left(\frac{\partial^2 T_1}{\partial x^2} + \frac{\partial^2 T_1}{\partial y^2}\right), \tag{2.4}$$

where c_p is the specific heat and k denotes the conductivity.

(b) Boundary Conditions

The boundary conditions considered in this thesis can be classified into three categories. The first is of a rigid wall boundary. The second is of a liquid/gas interface, i.e., the free surface boundary. The last one is a moving and deforming liquid/solid interface condition. Let's elaborate the three cases in detail.

i) rigid wall -- $\partial\Omega_w$

The fluid boundary conditions are $u = 0$, $v = 0$ for stationary walls. For thermal boundary conditions we consider in this work two types. The walls can either be isothermal or adiabatic.

ii) liquid/gas interface (free surface) -- $\partial\Omega_{lg}$

The kinematic condition over the free surface states that

$$v = \frac{\partial h}{\partial t} + u\frac{\partial h}{\partial x}. \tag{2.5}$$

Balance of stresses acting on the free surface gives

$$\hat{n} \bullet \tau = - \frac{\sigma}{R}\hat{n} + (\hat{m} \bullet \nabla \sigma)\hat{m}, \tag{2.6}$$

where $\hat{n}$ denotes the unit vector normal to the surface, τ denotes the stress

tensor, i.e., for Newtonian fluids, $\tau_{ij} = -p\delta_{ij} + \mu(\frac{\partial v_i}{\partial x_j} + \frac{\partial v_j}{\partial x_i})$. $\hat{m}$ denotes the streamwise unit vector tangent to the surface, and R denotes the radius of curvature such that $\frac{L}{R} = -h''(1+h'^2)^{-3/2}$. In general, $\hat{n} = \frac{-h'\hat{i}+\hat{j}}{(1+h'^2)^{1/2}}$, and $\hat{m} = \frac{\hat{i}+h'\hat{j}}{(1+h'^2)^{1/2}}$, and primes denote derivatives with respect to x.

The normal component of the surface stress equation can be expressed by

$$p - \frac{\sigma}{R} = \frac{2\mu}{(1+h'^2)}\,[h'^2\,\frac{\partial u}{\partial x} + \frac{\partial v}{\partial y} - h'\,(\frac{\partial u}{\partial y} + \frac{\partial v}{\partial x})], \tag{2.7}$$

and the tangential component can be expressed by

$$\mu\,[(1-h'^2)\,(\frac{\partial u}{\partial y} + \frac{\partial v}{\partial x}) - 4h'\,\frac{\partial u}{\partial x}] = (1+h'^2)^{1/2}\,(\frac{\partial \sigma}{\partial x} + h'\,\frac{\partial \sigma}{\partial y}), \tag{2.8}$$

where $\sigma = \sigma_0 + \frac{\partial \sigma}{\partial T}\,(T-T_0)$, and $-\frac{\partial \sigma}{\partial T} = \text{constant} > 0$.

iii) liquid/solid interface (solidification front) -- $\partial\Omega_{ls}$

Let's now consider the changing of phase at the interface. Consider the differential control volume surrounding the phase boundary shown in Fig. 2.1. If v_1 and v_2 denote the velocities in the direction normal to the boundary and $N(t)$ is the position of the boundary, the equation of conservation of mass can be expressed as

$$\rho_2(v_2 - \frac{dN}{dt}) - \rho_1(v_1 - \frac{dN}{dt}) = 0, \tag{2.9}$$

or, rearranging terms,

$$\rho_2 v_2 - \rho_1 v_1 = (\rho_2 - \rho_1)\,\frac{dN}{dt}\,, \tag{2.10}$$

where dN/dt is the boundary velocity in the normal direction, $\hat{n}$.

For simplicity, the interface is assumed to be massless, and thus without

momentum and energy. Let's make the free surface energy per unit area equal to the surface tension σ_s, then ignoring the normal viscous stress, the balance of the momentum in direction of the normal $\hat{n}$ becomes,

$$\rho_2(v_2 - \frac{dN}{dt})v_1 - \rho_1(v_1 - \frac{dN}{dt})v_1 = p_1 - p_2 - \frac{\sigma_s}{r_c}, \tag{2.11}$$

where r_c denotes the radius of curvature measured from phase 1. For a double-curved surface, $\frac{1}{r_c}$ should be replaced by $(\frac{1}{r_{c1}} + \frac{1}{r_{c2}})$, where both r_{c1} and r_{c2} denote the principal radii of curvature measured from phase 1. Since momentum fluxes are negligible for slow phase changes that are controlled by heat transfer, any pressure difference across the interface is generated from surface curvature. Such pressure differences, however, are significant only when the values of curvature, $\frac{1}{r_c}$, is large. These cases are beyond our concern in this thesis. The momentum equation, equation (2.11), then reduces to $p_1 = p_2 = p_s$, where p_s is the interface pressure. The balance of momentum in the direction of tangent $\hat{s}$ now yields (Fig. 2.2),

$$\rho_2(v_2 - \frac{dN}{dt})v_{2(s)} - \rho_1(v_1 - \frac{dN}{dt})v_{1(s)} = \tau_{1(s)} - \tau_{2(s)} + \frac{\partial \sigma_s}{\partial s}, \tag{2.12}$$

where the subscript, s refers to components of velocity and stress in s-direction. The tangential velocity is continuous by the continuum hypothesis

$$v_{1(s)} = v_{2(s)}, \tag{2.13}$$

and in view of equation (2.11) and for uniform surface tension, shear stress is also continuous, i.e.,

$$\tau_{1(s)} = \tau_{2(s)}. \tag{2.14}$$

Lastly, including flux of displacement power by pressure in the enthalpy flow, the balance of thermal energy becomes

$$\rho_2(v_2 - \frac{dN}{dt})h_2 - \rho_1(v_1 - \frac{dN}{dt})h_1 = q_1 - q_2, \tag{2.15}$$

which by employing equation (2.10) may be rearranged as

$$\rho_1(v_1 - \frac{dN}{dt})h_{12} = q_1 - q_2, \tag{2.16}$$

where $h_{12}=h_2 - h_1$ denotes the latent heat of phase change. For diffusional heat transfer in Fourier continua, equation (2.16) becomes

$$\rho_1(v_1 - \frac{dN}{dt})h_{12} = -k_1(\frac{\partial T_2}{\partial n})_s + k_2(\frac{\partial T_2}{\partial n})_s, \tag{2.17}$$

and for Newtonian fluids, equation (2.14) gives

$$\mu_1(\frac{\partial v_{1(s)}}{\partial n})_s = \mu_2(\frac{\partial v_{2(s)}}{\partial n})_s. \tag{2.18}$$

In addition to the foregoing boundary conditions, the assumption of local equilibrium implies phase equilibrium at the boundary, yielding a unique relation between temperature and pressure

$$T_s = T_s(p_s). \tag{2.19}$$

This same assumption gives $p_1 = p_2$.

(c) Non-dimensionalization Scheme

The non-dimensionalization scheme is different for each case considered in this thesis. We will discuss each one separately in Chapter IV, along with the results.

(d) Problem Definition

The geometries of the four cases studied are illustrated in Fig. 2.3 (a-d). For simplicity, these four cases will be denoted as TC1 (thermocapillary convection in a shallow cavity with adiabatic top free surface and differentially heated side walls), TC2 (thermocapillary convection in a shallow cavity with top free surface, imposed temperature distribution at the free surface, and periodic

side boundaries), S1 (solidification in a closed shallow cavity), and TCS1 (thermocapillary convection with phase change in a square open cavity). Case by case nondimensionalized boundary conditions are presented in Chapter IV.

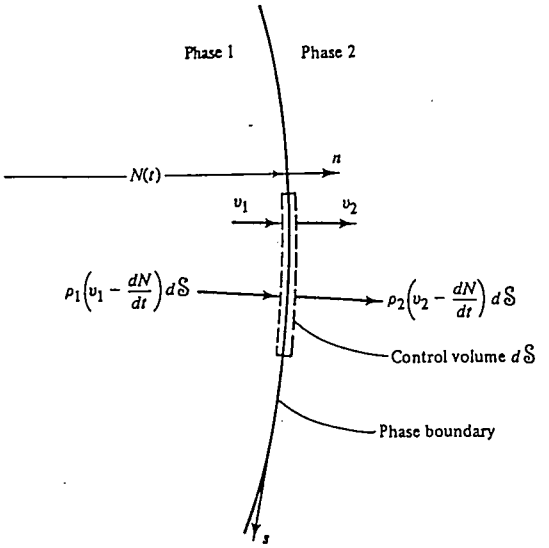

Fig. 2.1 Conservation of mass at phase boundary.

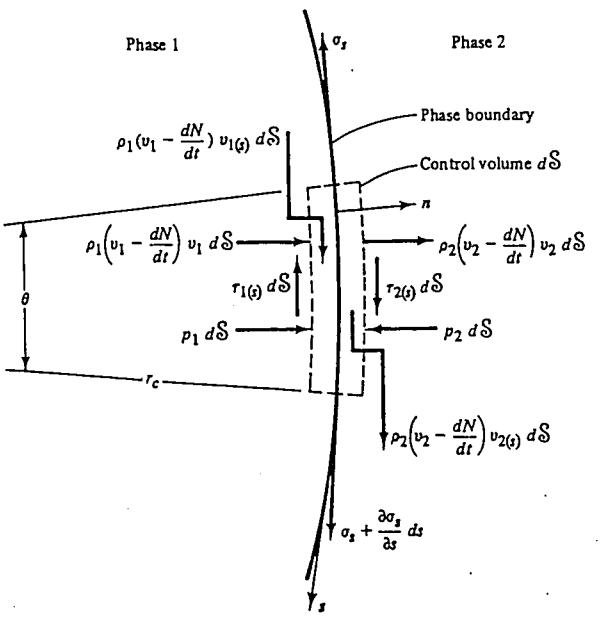

Fig. 2.2 Balance of momentum in $\hat{n}$ and $\hat{s}$ at phase boundary.

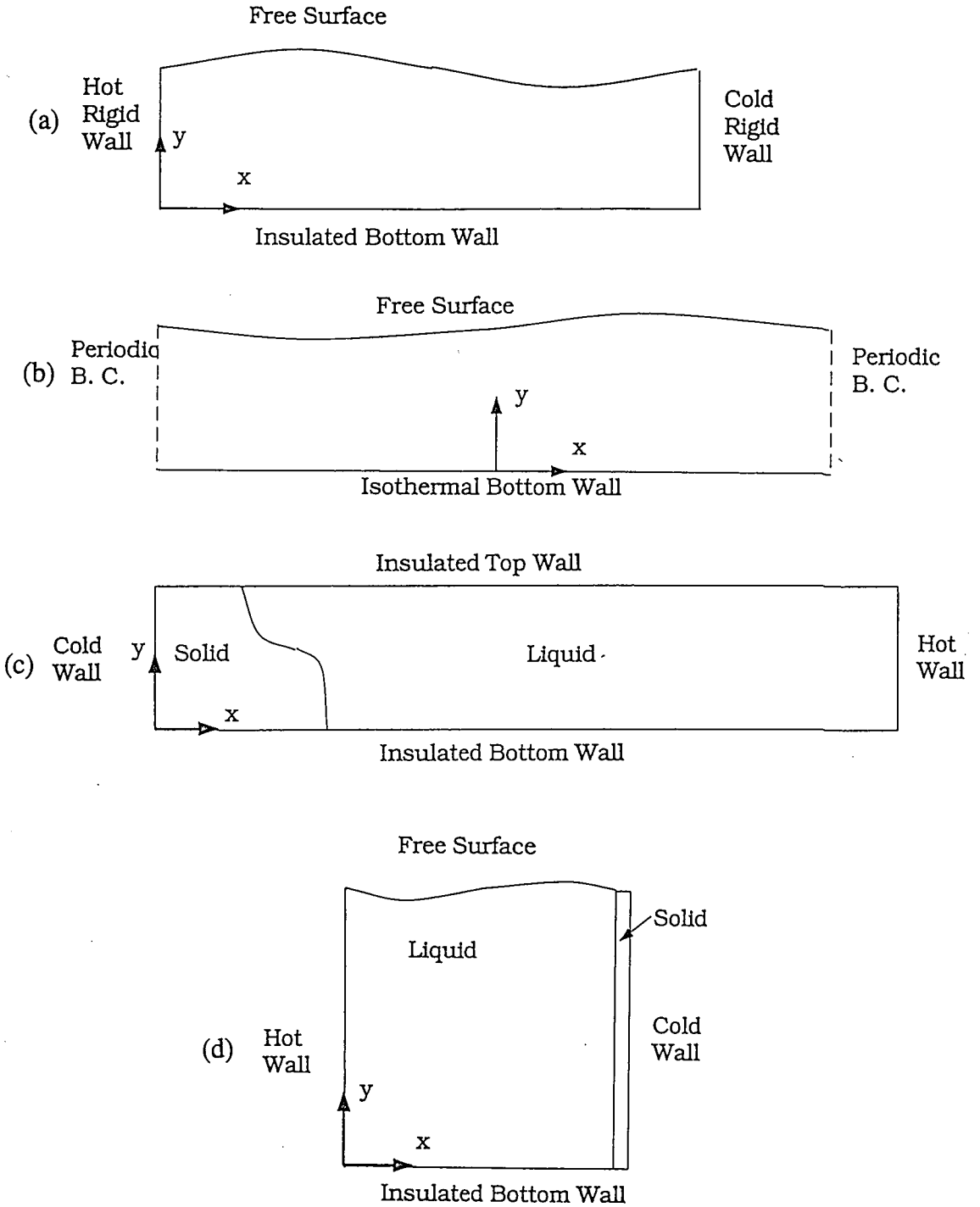

Fig. 2.3 (a-d) Geometries of the four cases.

Once the geometry and the parameters are determined for the problem of interest, the simulation is carried out using Nekton, a fluids spectral element software package developed recently at the Massachusetts Institute of Technology by A. Patera and his collaborators. This package takes in input geometry and values of parameters, and then uses a high-order finite-element method to solve the appropriate initial boundary value problem. Details of the two principle methods that the package uses, the spectral method and the arbitrary-Lagrangian-Eulerian method, are explained below.

(a) Spectral Method

The spatial discretization is based on a high-order finite element method, the spectral element method, for partial differential equations. The computational domain here is represented as a set of macro-elements with the solution and geometry being approximated by high-order polynomial expansions within each macro-element. While maintaining the geometric flexibility of low-order finite-element techniques, this approach offers high-order accuracy.

For two-dimensional domains, as all our cases are, the isoparametric spectral element spatial discretization proceeds by first breaking the two-dimensional domain into quadrangles, which we call "macro-" or "spectral" elements. Within each element, a local Cartesian mesh is constructed corresponding to NxN tensor-product Gauss-Lobatto Legendre collocation points. The Gauss-Lobatto points are clustered near elemental boundaries, and are

chosen because of their accurate approximation, interpolation and quadrature properties.

Within each element the dependent variables are expanded in terms of (N-1)th order tensor-product (polynomial) Lagrangian interpolants through the Gauss-Lobatto Legendre collocation points, as similar to the standard finite element techniques. For an example, the temperature is expanded as $T=\Sigma_i T_i h_i$, where the h_i are Lagrangian interpolants and the T_i are nodal values of the temperature.

The semi-discrete equations are generated using the so called weighted-residual techniques, corresponding to inserting the assumed forms for the dependent variables (e.g., $T=\Sigma_i T_i h_i$) into the governing equations, and requiring that the resulting residual vanish in some integral, weighted sense. We have to note that here, since the basis functions chosen are Lagrangian interpolants, the numerical variables that are solved for (e.g., the T_i), correspond to the values of the function of interest (e.g., the temperature) at the collocation points of the mesh.

Convergence to the exact solution is obtained either by increasing the number of macro-elements, K, or by increasing the order of the interpolants, N, in elements of fixed identity. In the case of using K, the error decreases algebraically like K^{-N}. In the case of using N, the error decreases exponentially by the order of $e^{-\alpha N}$, for smooth solutions. As always, any solution obtained numerically should be verified to be convergent by repeating the calculation with higher K or N.

The stability restriction (Courant or CFL condition) can be written in the

form

$$\Delta t < C \text{ x } Min_{DF} \{\frac{\Delta x}{|u_x|}, \frac{\Delta y}{|u_y|}, \frac{\Delta z}{|u_z|}\}, \tag{3.1}$$

where C is the Courant number, Δx, Δy, Δz are the x, y, z distances between the spatial collocation points, u_x, u_y, u_z are the x, y, z velocities, respectively. Min_{DF} refers to the minimum over the entire flow field. The Courant number is usually a default value set by the package, the program ensures that the Courant condition is satisfied. If necessary, the Courant number can be easily modified to satisfy the user's need.

The stability restriction used for surface tension effects is

$$\Delta t < Min_{\partial D} [\frac{\rho}{\sigma} (\frac{\Delta s}{\pi})^3]^{1/2}, \tag{3.2}$$

where ρ is the fluid density, Δs is the curvilinear distance between the spatial collocation points on the surface tension boundary ∂D, σ is the surface tension coefficient, and $Min_{\partial D}$ refers to the minimum over the surface tension boundary.

The advantage of using the spectral element methods, rather than low-order finite element methods, is that the increased coupling introduced by high-order methods increases the work only algebraically, whereas the increase in accuracy is exponential. These arguments only apply for problems with smooth solutions. However, with the exception of boundary-induced singularities, incompressible flow and heat transfer problems will generally satisfy this requirement.

(b) ALE (Arbitrary-Lagrangian-Eulerian) Method

The ALE method is applicable for solving the Navier-Stokes equations of

flows at all speeds. This method is both Lagrangian and Eulerian, and it uses a finite difference mesh with vertices that may move with the fluid (Lagrangian), be held fixed (Eulerian), or be moved in any other prescribed way. Because of this flexibility the method is referred to as an Arbitrary-Lagrangian-Eulerian technique. The advantages of using the ALE method include its ability to resolve arbitrary confining boundaries, to have variable zoning for purposes of obtaining optimum resolution, to be almost Lagrangian for improved accuracy in problems where fully Lagrangian calculations are not possible, and to operate with time steps many times larger than possible with explicit methods.

The finite difference mesh used here consists of a network of quadrilateral cells with vertices labeled by integer pairs (i, j), denoting column i and row j. Fluid variables are assigned to staggered locations in the mesh as shown in Figure 6. Pressures (p), specific internal energies (I), cell volumes (V), and densities (ρ) or masses (M) are all assigned to cell centers. Coordinates (x, y) and velocity components (u, v) are assigned to cell vertices.

The differential equations to be solved are

$$\frac{\partial \rho}{\partial t} + \nabla \bullet \rho \boldsymbol{u} = 0, \tag{3.3}$$

$$\frac{\partial \rho \boldsymbol{u}}{\partial t} + \nabla \bullet \rho \boldsymbol{u}\boldsymbol{u} = - \nabla p + \rho \boldsymbol{g}, \tag{3.4}$$

$$\frac{\partial \rho E}{\partial t} + \nabla \bullet \rho E \boldsymbol{u} = -\nabla \bullet p \boldsymbol{u} + \rho \boldsymbol{g} \bullet \boldsymbol{u}, \tag{3.5}$$

where $E = \frac{1}{2}\boldsymbol{u} \bullet \boldsymbol{u} + I$, and I is the material specific internal energy. In equations (3.4) and (3.5), g is a body acceleration (usually gravity) and p is the fluid pressure given by the equation of state

$$p = f(\rho, I). \tag{3.6}$$

The conservation statements of mass, momentum, and energy contained in

equations (3.3) to (3.5) are more convenient for our purposes when integrated over a volume, V, which may be moving with an arbitrarily prescribed velocity. Denoting the surface of V by S and the outward normal on S by $\boldsymbol{n}$, these equations become

$$\frac{d}{dt}\int_v \rho dV - \int_s \rho(\boldsymbol{U}-\boldsymbol{u}) \circ \boldsymbol{u}\, dS = 0, \tag{3.7}$$

$$\frac{d}{dt}\int_v \rho \boldsymbol{u} dV - \int_s \rho \boldsymbol{u}(\boldsymbol{U}-\boldsymbol{u}) \circ \boldsymbol{n} dS + \int_v \nabla p dV - \int \rho \boldsymbol{g} dV = 0, \tag{3.8}$$

$$\frac{d}{dt}\int_v \rho E dV - \int_s \rho E(\boldsymbol{U}-\boldsymbol{u}) \circ \boldsymbol{n} dS + \int_s p\boldsymbol{u} \circ \boldsymbol{n} dS - \int_v \rho \boldsymbol{g} \circ \boldsymbol{u} dV = 0, \tag{3.9}$$

where in these expressions, $\boldsymbol{U}$ is the velocity of the surface S. When $\boldsymbol{U} = 0$, the equations are Eulerian, and when $\boldsymbol{U} = \boldsymbol{u}$, the equations are Lagrangian. The pressure gradient term in equation (3.8) could be written as a surface integral, but for cylindrical coordinates a simpler finite difference approximation is obtained directly from the volume integral and this is advantageous for the implicit formulation of the difference equations.

The calculations necessary to advance a solution one step in time, δt, are separated into three distinct phases. The first phase consists of an explicit Lagrangian calculation, except mesh vertices are not moved. Second, an iteration phase adjusts the pressure gradient forces to the advanced time level. This phase, which is optional, eliminates the usual Courant-like numerical stability condition that limits sound waves to travel no further than one cell per time step. The mesh vertices are moved to their new Lagrangian positions after this phase. Finally, in the third phase, which is also optional, the mesh can be moved to a new configuration. In this (rezone) phase, convective fluxes must be

computed to account for the movement of fluid between cells as the mesh moves. The calculations in this last phase are automatically iterated if zones try to move too far in any single step, so that gross rezoning can be accomplished without introducing numerical instabilities.

This separation of a calculational cycle into a Lagrangian phase and a convective flux, or rezone phase has been used in many hydrodynamics computer codes. In the present technique the different phases can be combined in various ways to suit the requirements of individual problems. Phase one and three are variations of familiar Lagrangian and Eulerian finite difference techniques. The phase two iteration, however, is new and requires some preliminary discussion. The purpose of phase two is to get time-advanced pressure forces in the Lagrangian part of a calculation. The reason for this can be appreciated from the following argument. In an explicit method pressure forces can be transmitted only one cell each time step, that is, cells exert pressure forces only on neighboring cells. When the time step is chosen so large that sound waves should travel more than one cell, the one cell limitation is clearly inaccurate and a catastrophic instability develops. The instability arises because the explicit pressure gradients lead to excessive cell compressions or expansions when multiplied by too large a time step. This then leads to larger pressure gradients the next cycle, which try to reverse the previous excesses, but since the time step is too large the reversal is also too large and the process repeats itself with a rapidly increasing amplitude. The over-response to pressure gradients in this fashion is eliminated by using time-advanced pressure gradients, for then cells cannot compress or expand to the point where the gradients are reversed.

Unfortunately, the time-advanced pressures depend on the accelerations and velocities computed from those pressures, so an iterative solution of the equations is necessary. Physically, an iteration offers a means by which pressure signals can traverse across more than one cell in a time step. The iteration is, however, more efficient than a straight explicit calculation with reduced time step, because pressure variations are propagated only to the point where they are producing effects no longer considered significant.

IV. RESULTS

In this chapter we will present the results of numerical simulations for each problem defined in Chapter II (d) separately, and then give final remarks on all four cases.

(a) Problem TC1

In this problem, a study of the transient characteristics of thermocapillary convection in an open rectangular cavity (Fig. 2.3 (a)) is conducted. The following reference quantities are introduced in order to non-dimensionalize the governing equations

$$x^*=\frac{x}{L_{ref}},\ y^*=\frac{y}{L_{ref}},\ u^*=\frac{u}{u_{ref}},\ v^*=\frac{v}{u_{ref}},\ p^*=\frac{pL_{ref}}{\mu u_{ref}},\ \theta^*=\frac{T\text{-}T_0}{\Delta T_{ref}},\ t^*=\frac{u_{ref}t}{L_{ref}}.$$

The governing equations then become

$$\frac{\partial u^*}{\partial x^*}+\frac{\partial v^*}{\partial y^*}=0, \tag{4.1}$$

$$Re\,(\frac{\partial u^*}{\partial t^*}+u^*\frac{\partial u^*}{\partial x^*}+v^*\frac{\partial u^*}{\partial y^*})=-\frac{\partial p^*}{\partial x^*}+\frac{\partial^2 u^*}{\partial x^{*2}}+\frac{\partial^2 u^*}{\partial y^{*2}}, \tag{4.2}$$

$$Re\,(\frac{\partial v^*}{\partial t^*}+u^*\frac{\partial v^*}{\partial x^*}+v^*\frac{\partial v^*}{\partial y^*})=-\frac{\partial p^*}{\partial y^*}+\frac{\partial^2 v^*}{\partial x^{*2}}+\frac{\partial^2 v^*}{\partial y^{*2}}, \tag{4.3}$$

$$Ma\,(\frac{\partial \theta^*}{\partial t^*}+u^*\frac{\partial \theta^*}{\partial x^*}+v^*\frac{\partial \theta^*}{\partial y^*})=\frac{\partial^2 \theta^*}{\partial x^{*2}}+\frac{\partial^2 \theta^*}{\partial y^{*2}}, \tag{4.4}$$

where $Re=\frac{u_{ref}L_{ref}}{\nu}$,

$$Pr = \frac{\nu}{\alpha},$$

and $Ma = RePr.$

Using the horizontal length of the cavity as the characteristic length, L_{ref}, the dimensionless boundary conditions for this problem are

$u^*(0,y^*,t^*)=0$, $v^*(0,y^*,t^*)=0$, $\theta^*(0,y^*,t^*)=1$;

$u^*(1,y^*,t^*)=0$, $v^*(1,y^*,t^*)=0$, $\theta^*(1,y^*,t^*)=0$;

$u^*(x^*,0,t^*)=0$, $v^*(x^*,0,t^*)=0$, $\frac{\partial\theta^*}{\partial y^*}(x^*,0,t^*)=0$;

and at y^*=0.25, free surface conditions ($\partial\Omega_{lg}$).

We will now discuss the dimensionless free surface conditions, $\partial\Omega_{lg}$. The kinematic condition at the free surface is

$$v^* = \frac{\partial h^*}{\partial t^*} + u^* \frac{\partial h^*}{\partial x^*}. \tag{4.5}$$

In modeling thermocapillarity, the surface tension is assumed to decrease linear with increasing temperature, thus,

$$\sigma = \sigma_0 - \gamma\,(T - T_0), \tag{4.6}$$

where $\gamma = -\frac{d\sigma}{dT}$ = constant > 0.

When thermocapillarity is the dominant mechanism driving the flow, the characteristic speed is naturally

$$u_{ref} = \frac{\gamma\Delta T}{\mu}, \tag{4.6a}$$

and the dimensionless surface tension is

$$\sigma^* = S - T^*,$$

where $S = \frac{\sigma_0}{\gamma\Delta T}$ is the surface tension number. Also used in this thesis is the capillary number, $Ca = \frac{1}{S}$. With the above definition of u_{ref}

$$Re = \frac{\gamma \Delta T L_{ref}}{\mu \nu}, \tag{4.6b}$$

and thus,

$$Ma = \frac{u_{ref} L_{ref}}{\alpha} = \frac{\gamma \Delta T L_{ref}}{\alpha \mu}.$$

Introducing the static Bond number, $Bo = \frac{\rho_0 g L^2}{\sigma_0}$, the normal and the tangential components of the surface stress equation in nondimensional form become

$$p^* - \frac{\sigma^*}{R^*} - BoSh^* + \text{constant} = -\left(\frac{2}{1+h'^{*2}}\right)\left[(1-h'^{*2})\frac{\partial u^*}{\partial x^*} + h'^*\left(\frac{\partial u^*}{\partial y^*} + \frac{\partial v^*}{\partial x^*}\right)\right], \tag{4.7}$$

and

$$(1-h'^{*2})\left(\frac{\partial u^*}{\partial y^*} + \frac{\partial v^*}{\partial x^*}\right) - 4h'^*\frac{\partial u^*}{\partial x^*} = -(1+h'^{*2})^{1/2}\left(\frac{\partial T^*}{\partial x^*} + h'^*\frac{\partial T^*}{\partial y^*}\right), \tag{4.8}$$

at $y^* = A + h^*$. The unspecified constant in equation (4.7) represents the dimensionless pressure difference between the liquid and the gas in the static state. If the free surface is very flat, i.e., $h'^{*2} << 1$, equations (4.7) and (4.8) may be approximated by

$$p^* + h''^*(S - T^*) - BoSh^* + \text{constant} = 2\frac{\partial v^*}{\partial y^*} + 2h'^*\left(\frac{\partial u^*}{\partial y^*} + \frac{\partial v^*}{\partial x^*}\right), \tag{4.9}$$

and

$$\left(\frac{\partial u^*}{\partial y^*} + \frac{\partial v^*}{\partial x^*}\right) - 4h'^*\frac{\partial u^*}{\partial x^*} = -\frac{\partial T^*}{\partial x^*} - BiT^*h'^*. \tag{4.10}$$

The aspect ratio (height/length) in this problem is 0.25, while the Prandtl number is 0.015. The capillary number equals to 0.01. Bo is 0.0 since g is zero in this case. Bi is 0.0 because the free surface is adiabatic. Simulation is carried out for Reynolds number equals to 7200, based on equation (4.6b). Plots of isotherms and streamlines are shown in Figs. 4.1 and 4.2. From Fig. 4.1, we can see not only the temperature distribution pattern, but also the deformed free surface shape at various times. We notice that both at the free surface and the

bottom wall, the temperature lines are normal to these boundaries. This is correct since the free surface and the bottom wall are both adiabatic (insulated), i.e., $\frac{\partial T}{\partial \eta} = 0$, where η denotes distances normal to the surface. In a case where there is no free surface deformation, the isotherms may be parallel to each other and show a uniform distribution when convection is weak. But in our problem, because of the surface deformation and the strong free convection effects inside the cavity, the temperature lines are all tilted and curved. We notice that the isotherms have the most amount of bend at the cold side, where the convection effect is larger.

The streamfunction is defined by

$$u = \frac{\partial \psi}{\partial y}, \; v = - \frac{\partial \psi}{\partial x},$$

and like u and v, $\psi = 0$ at the solid walls. Instantaneous streamline patterns are shown in Fig. 4.2. As time elapses, vortices are generated and then disappear as the trough and peak of the deformed free surface move. It is not very easy though, to find an obvious pattern with how the vortices behave.

The free surface oscillates through the transient period. The peak of the wave moves from the hot wall to the cold wall, and then get bounced back from the cold wall to the hot wall. This waviness eventually damps out and the surface becomes near-flat again. This whole process takes about 540 dimensionless time units.

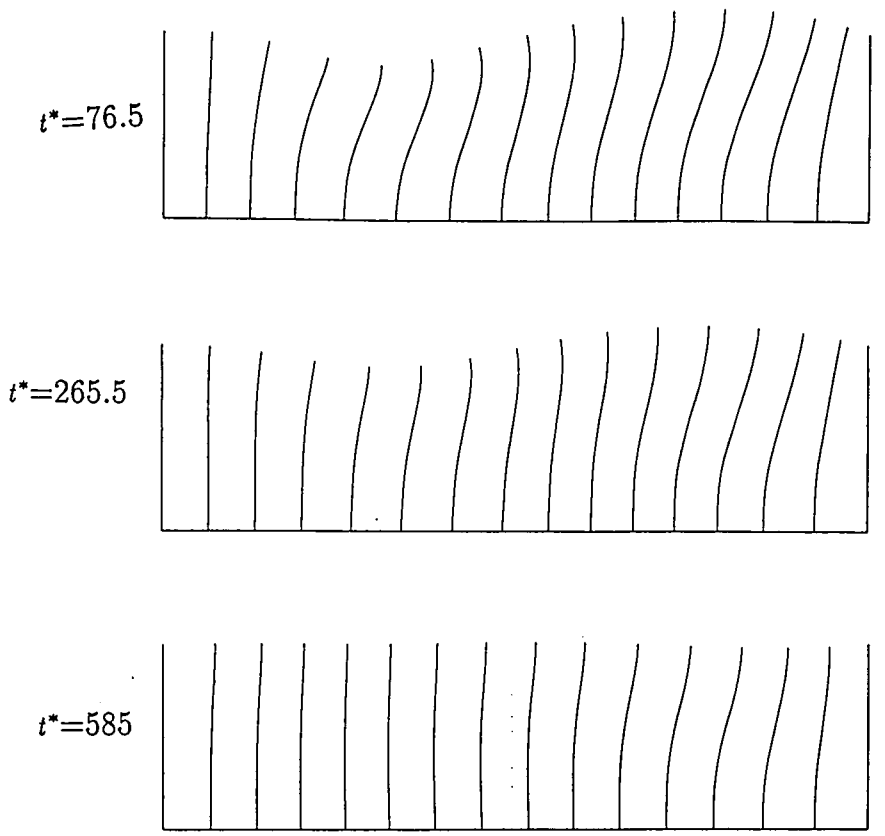

Fig. 4.1 Problem TC1--Instantaneous isotherms.

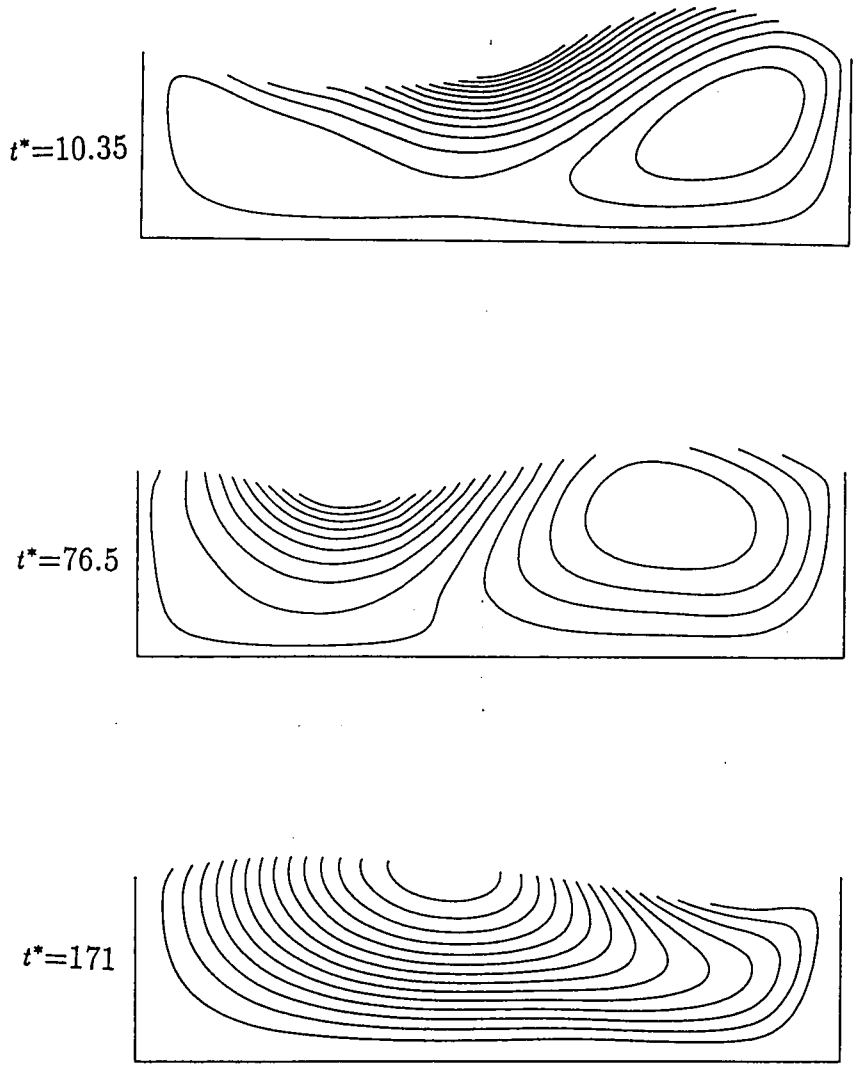

Fig. 4.2 Problem TC1--Instantaneous streamlines.

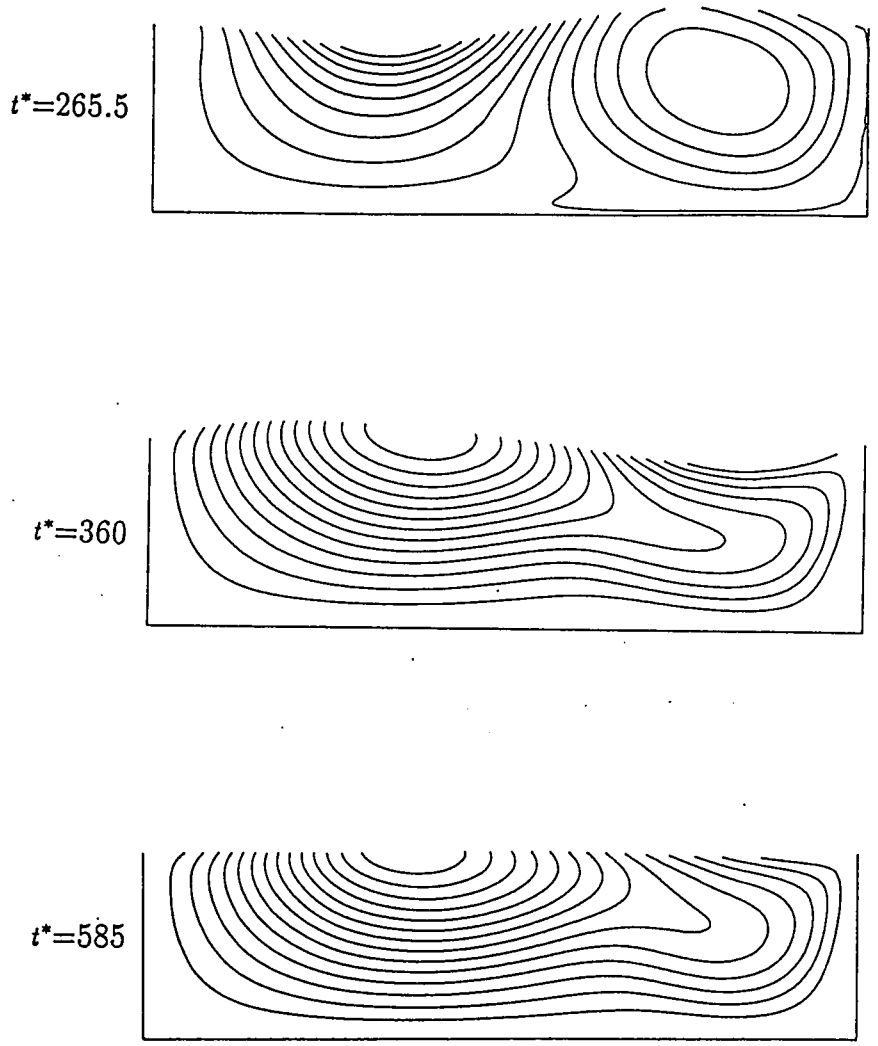

Fig. 4.2 (cont.) Problem TC1--Instantaneous streamlines.

(b) Problem TC2

In this problem, we study thermocapillary convection in an open shallow cavity. Upon the top free surface, there is an imposed periodic in space temperature distribution (Fig. 2.3(b)). Instead of modeling the whole cavity domain, which is extremely computationally intensive, we use a cell with periodic boundary conditions on the side boundaries. This is a good model as long as we are not interested in the end effects. The temperature function is defined such that it gives the highest temperature at the mid-span of the surface and decreases exponentially as it approaches the vertical sides of the computational domain. The aspect ratio of the computational domain is 0.2 in this problem. The Prandtl number equals 0.01. The free surface is flat in this case, since the Capillary number is set to be small ($Ca = 0.01$). Simulations are carried out for Reynolds numbers, based on equation (4.6b), in the range from 100 to 50,000. All solutions are time-independent as $t \to \infty$ in the range of the Reynolds numbers considered.

The mathematical model for this problem consists of equations (4.1) to (4.4), with dimensionless boundary conditions

$u^*(-0.5,y^*,t^*)=u^*(0.5,y^*,t^*)$, $v^*(-0.5,y^*,t^*)=v^*(0.5,y^*,t^*)$, $\theta^*(-0.5,y^*,t^*)=\theta^*(0.5,y^*,t^*)$;

$u^*(x^*,0,t^*)=0$, $v^*(x^*,0,t^*)=0$, $\theta^*(x^*,0,t^*)=0$;

$\theta(x^*,0.2,t^*)=exp(-9x^{*2})$, and free surface conditions ($\partial\Omega_{lg}$), equations (4.5) to (4.10).

Plots of isotherms for four different values of Reynolds number are shown

in Figs. 4.3(a), 4.4(a), 4.5(a) and 4.6(a). We can see that as the Reynolds number increases, the pattern of the isotherms does not seem to changes much, since Pr is small. However, the lower lines start to bend a little near the side walls at high Reynolds numbers (Fig. 4.6(a)).

Figs. 4.3(b), 4.4(b), 4.5(b) and 4.6(b) show the variation of streamline patterns with Reynolds number. The vortices shift to the cold sides and a thin shear layer develops at the free surface as the Reynolds number increases. The shape of the streamline contours change a great deal. For small values of Reynolds number, the contours appear to be elliptical, and for large value of Reynolds number, the contours are squeezed toward the side walls. As the Reynolds number reaches 50,000, we notice that there are two weak vortices developing. This flow structure is not observed in low Reynolds number cases.

Figs. 4.3(c), 4.4(c), 4.5(c) and 4.6(c) show the vorticity contours for various Reynolds numbers. Vorticity is defined by

$$\omega = \frac{\partial v}{\partial x} - \frac{\partial u}{\partial y} = -\nabla^2 \psi.$$

The vorticities are the largest at the cold corners where the imposed heat fluxes are the minimum. This can be seen in Fig. 4.6(c). Some ω-lines are broken or wrinkled due to insufficient numerical accuracy. As the Reynolds number increases, the isovorticity lines are all being pushed to the sides. As $Re \to \infty$, we observe that ω is constant inside the regions of closed streamlines, in accordance with the Prandtl-Batchelor theorem.

All of these plots show a symmetry about the centerline of the computational domain. This is true because the vertical boundaries are defined to be periodic with each other and the imposed temperature boundary conditions

are also symmetric functions, $\theta^*(-x^*)=\theta^*(x^*)$ for $0 \leq x^* \leq 0.5$. No evidence of breaking this symmetry was observed in the range of values of the Reynolds numbers studied.

Even though the free surface looks flat from the numerical simulation, as anticipated, small deformations are observable when plotted on the appropriate scale. From the plot of local y-displacement vs. x at the free surface (Fig. 4.7), it is obvious that a near-drop-shaped pattern represents the amplitude of the deformation for low Reynolds number cases. As the Reynolds number increases, this amplitude decreases.

Plots of speed vs. x at the free surface are shown in Fig. 4.8. As the Reynolds number increases, the magnitude of the dimensionless speed decreases. The shape of the curves again appear to be symmetric with the center line of the calculation domain. The maximum speeds occur at about one quarter and three quarters from the left-most boundary for low Reynolds numbers. In the cases of high Reynolds numbers, the points of maximum speeds shift towards the side boundaries, and the profiles become almost flat over a large portion of the free surface.

A third plot showing the free surface characteristics is the plot of pressure vs. x (Fig. 4.9). As the Reynolds number increases, the magnitude of the pressure on the free surface increases. These pressure curves also show that the pressure is the lowest at the mid-span of the interface and the highest at the ends of the cell for low Reynolds number cases. For high Reynolds numbers, the pressure drops at places close to the sides, and then increases dramatically.

Fig. 4.10 shows the average Nusselt number vs. Re at the bottom wall of

the computational domain. The average Nu calculated as $\overline{Nu} = \int \frac{\partial T^*}{\partial y^*}\, dx^*$ decreases slightly as the Re increases.

Fig. 4.11 (a) shows ${u^*}_{max}$ vs. Re as defined in equations (4.6a) and (4.6b). We can see from this plot that ${u^*}_{max}$ decreases as Re increases. This is due to the characteristic speed, u_{ref}, increasing by a greater proportion than does the actual speed, u, as Re increases.

We can alternatively define $u_{ref} = (\frac{\gamma^2 \Delta T^2 \nu}{\mu^2 L_{ref}})^{1/3}$, following Ostrach (1982). With this definition of u_{ref}, the ${u^*}_{max}$ vs. Re is shown in Fig. 4.11 (b). The relationship shows an increasing trend of ${u^*}_{max}$ as Re increases.

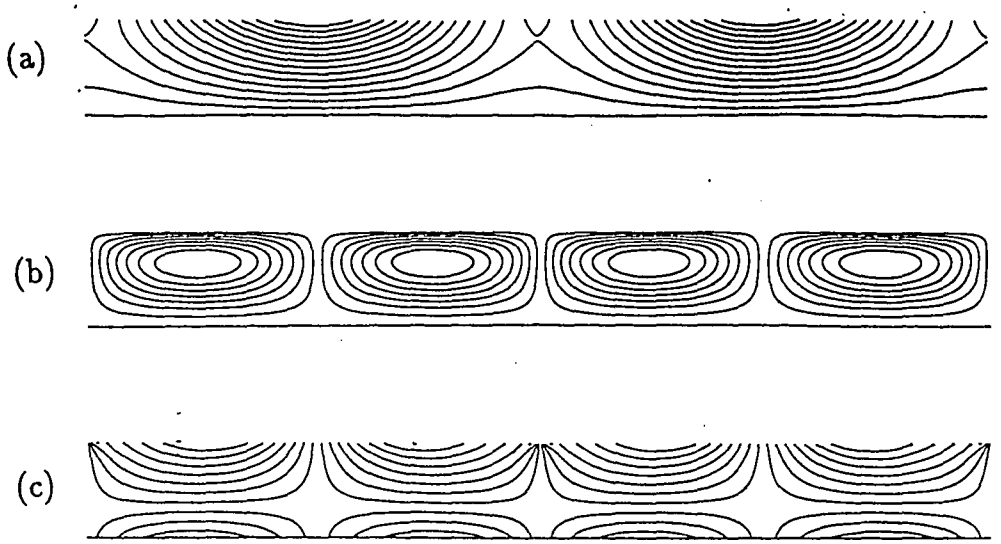

Fig. 4.3 Problem TC2--$Re = 100$

(a) Isotherms, (b) Streamlines, (c) Vorticity contours.

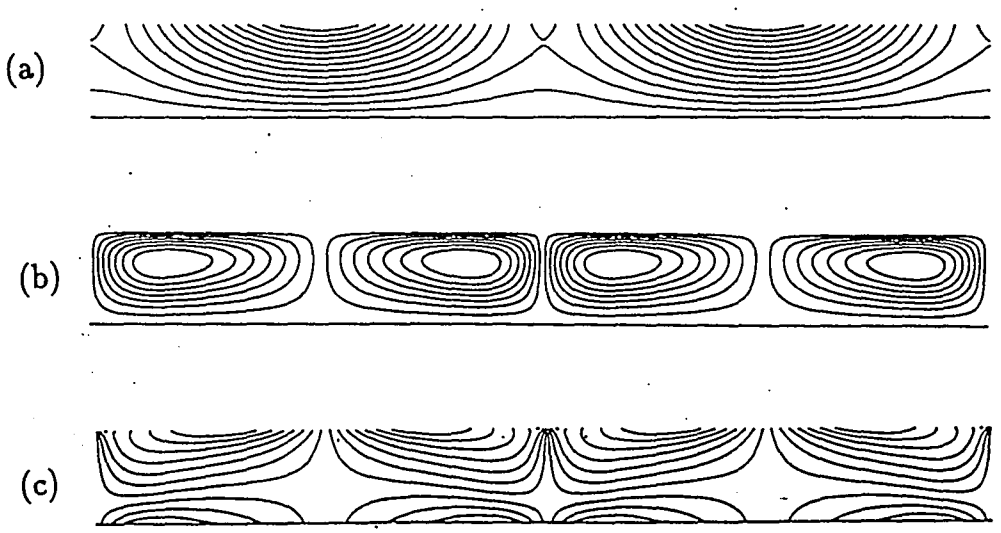

Fig. 4.4 Problem TC2--$Re = 1000$

(a) Isotherms, (b) Streamlines, (c) Vorticity contours.

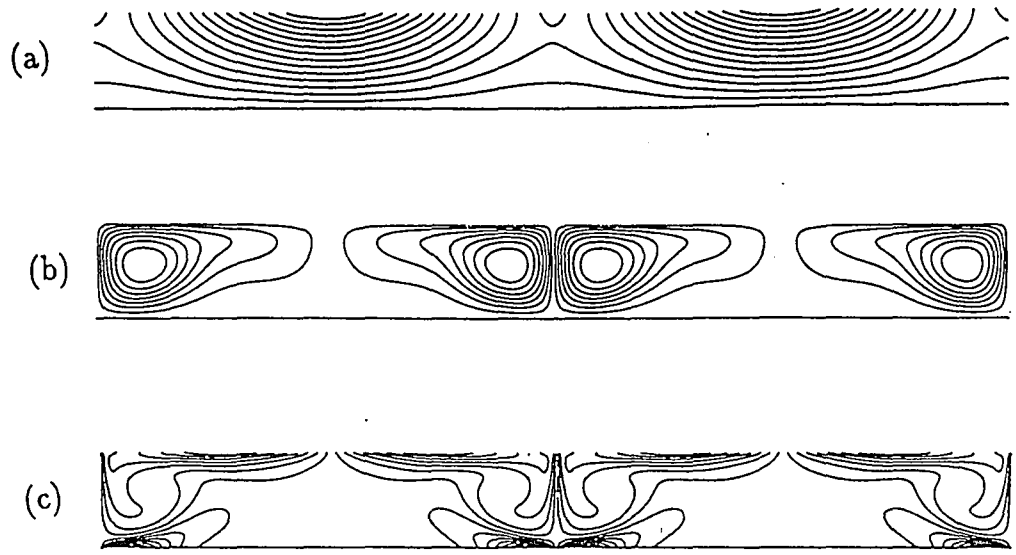

Fig. 4.5 Problem TC2--$Re = 10000$

(a) Isotherms, (b) Streamlines, (c) Vorticity contours.

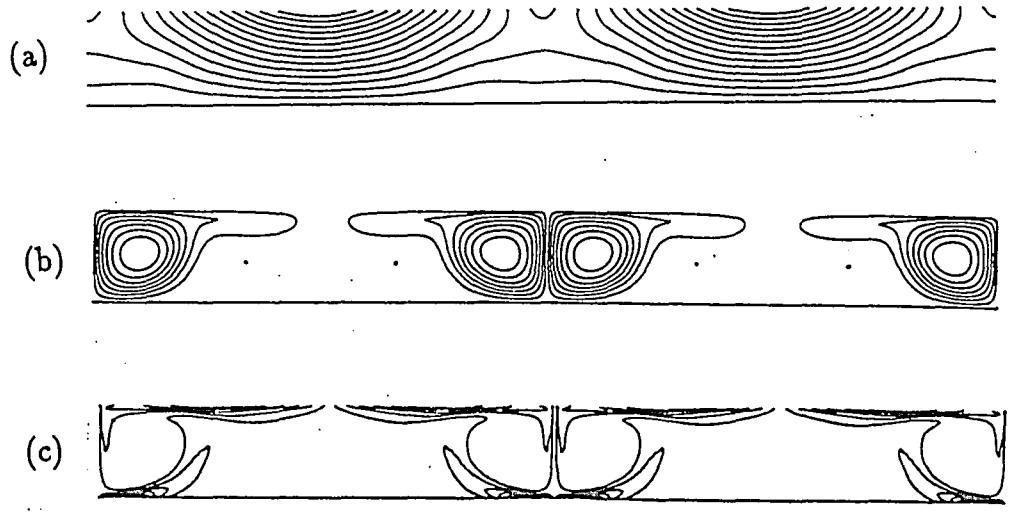

Fig. 4.6 Problem TC2--$Re = 50000$

(a) Isotherms, (b) Streamlines, (c) Vorticity contours.

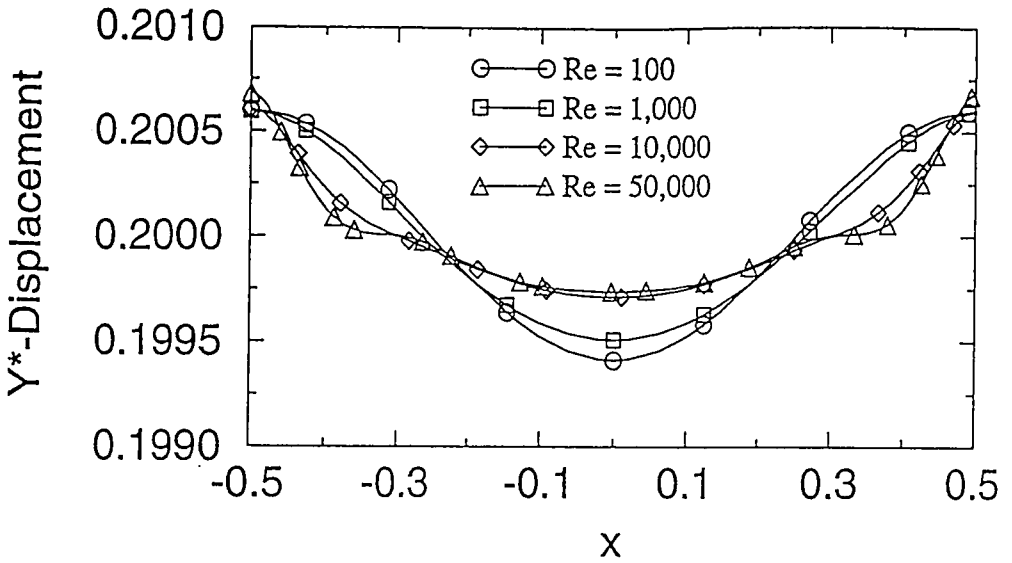

Fig. 4.7 Problem TC2--Free surface displacement.

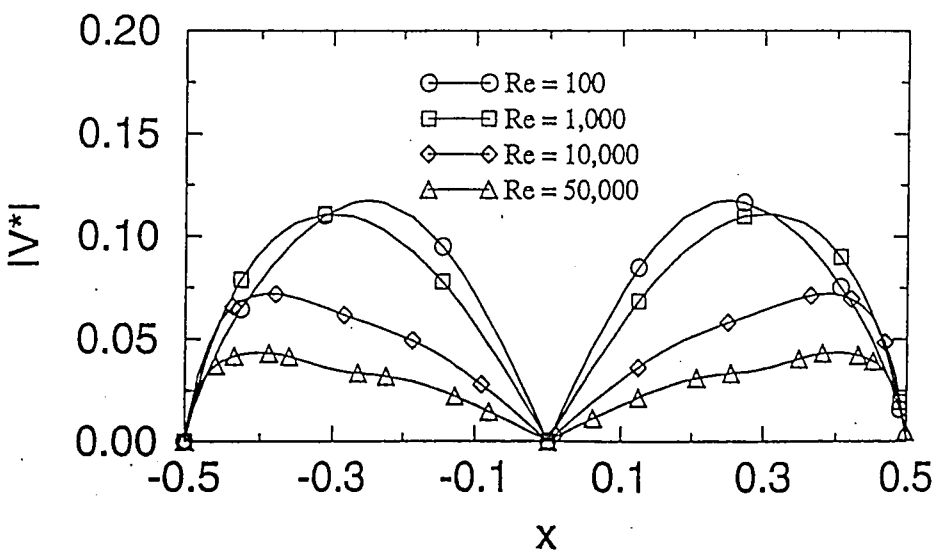

Fig. 4.8 Problem TC2--Speed vs. x at free surface.

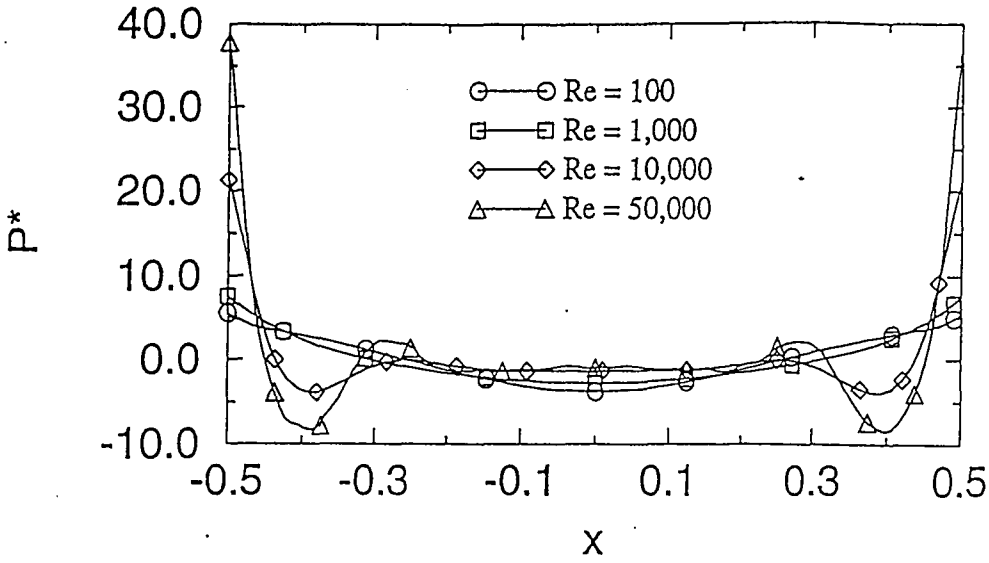

Fig. 4.9 Problem TC2--Pressure variation at free surface.

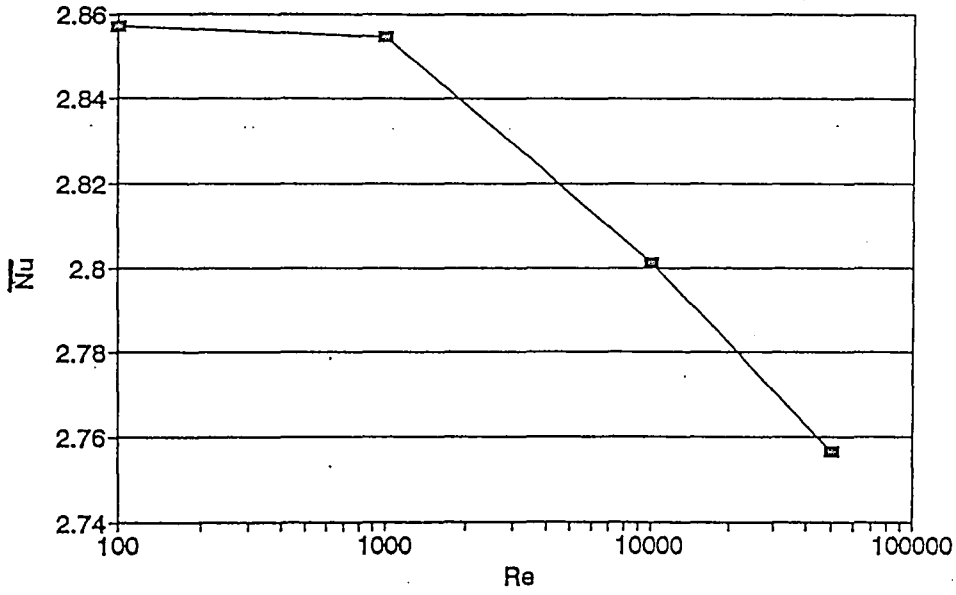

Fig. 4.10 Problem TC2--Average Nu at the bottom wall vs. Re.

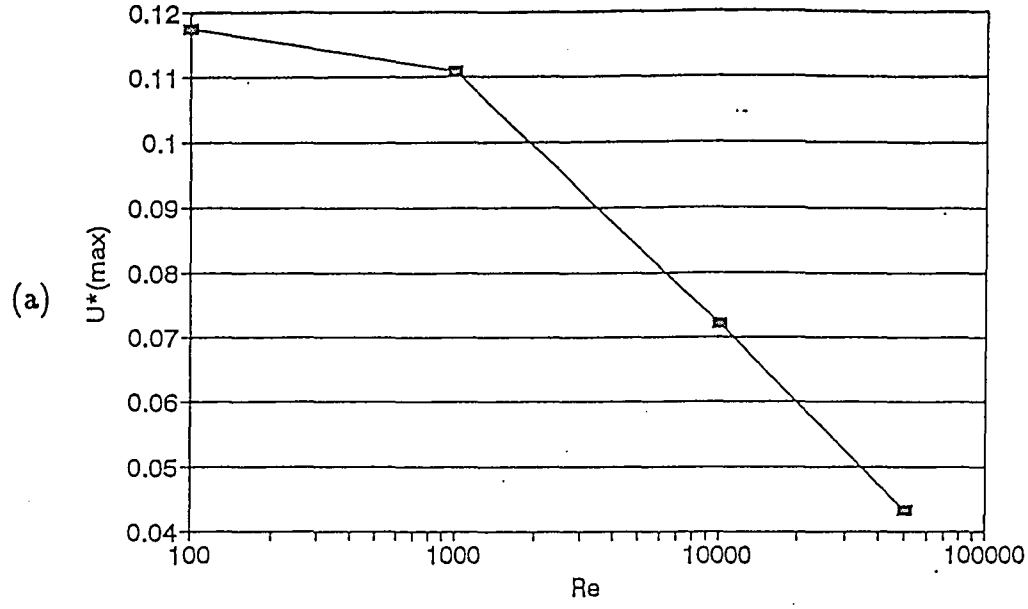

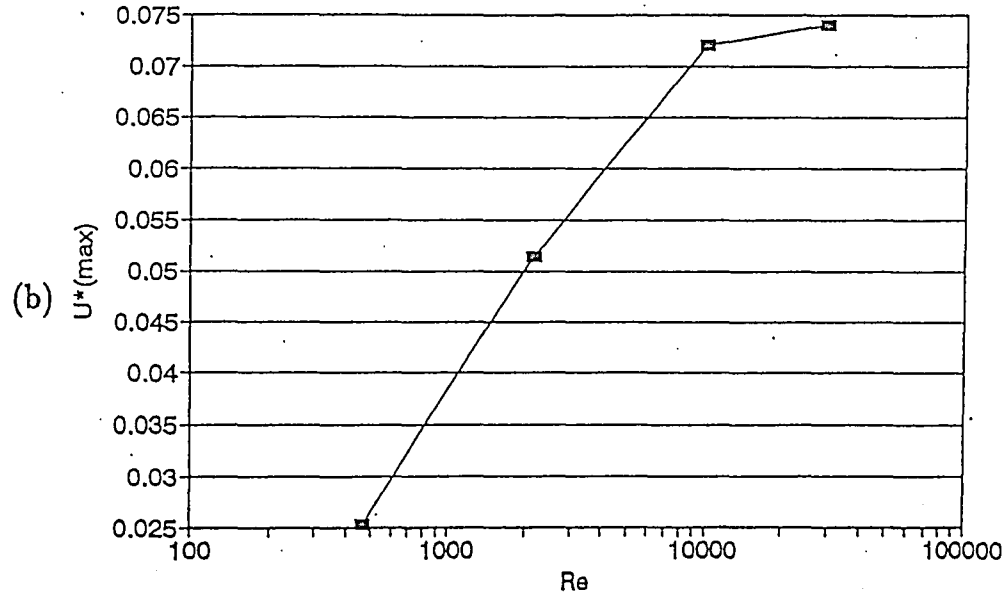

Fig. 4.11 Problem TC2--u^* vs. Re based on different scalings.

(a) $u_{ref} = \frac{\gamma \Delta T}{\mu}$, (b) $u_{ref} = (\frac{\gamma^2 \Delta T^2 \nu}{\mu^2 L_{ref}})^{1/3}$.

(c) Problem S1

In this problem, a simple solidification process is simulated. Our computational domain is a closed shallow rectangular cavity (Fig. 2.3 (c)). The left side of the cavity contains a small portion of solid material maintained at a temperature much lower than the freezing/melting temperature, T_f. The right side of the cavity is kept at a temperature above T_f. Both the top and bottom walls are kept insulated.

We use the following set of reference quantities to non-dimensionalize the governing equations in the liquid phase

$$x^*=\frac{x}{L_{ref}},\ y^*=\frac{y}{L_{ref}},\ u^*=\frac{u}{u_{ref}},\ v^*=\frac{v}{u_{ref}},\ p^*=\frac{pL}{\mu u_{ref}},\ \theta^*=\frac{T\text{-}T_0}{\Delta T_{ref}},\ t^*=\frac{u_{ref}t}{L},$$

where L_{ref} is the height of the cavity, $u_{ref} = \frac{\alpha}{l}$, and $\Delta T_{ref} = T_f$ - T_c. The governing equations then become

$$\frac{\partial u^*}{\partial x^*} + \frac{\partial v^*}{\partial y^*} = 0, \tag{4.11}$$

$$Re\ (\frac{\partial u^*}{\partial t^*} + u^*\frac{\partial u^*}{\partial x^*} + v^*\frac{\partial u^*}{\partial y^*}) = -\frac{\partial p^*}{\partial x^*} + \frac{\partial^2 u^*}{\partial x^{*2}} + \frac{\partial^2 u^*}{\partial y^{*2}}, \tag{4.12}$$

$$Re\ (\frac{\partial v^*}{\partial t^*} + u^*\frac{\partial v^*}{\partial x^*} + v^*\frac{\partial v^*}{\partial y^*}) = -\frac{\partial p^*}{\partial y^*} + \frac{\partial^2 v^*}{\partial x^{*2}} + \frac{\partial^2 v^*}{\partial y^{*2}} + \frac{Gr}{Re}\,\theta^*\ , \tag{4.13}$$

$$Re\ Pr\ (\frac{\partial \theta^*}{\partial t^*} + u^*\frac{\partial \theta^*}{\partial x^*} + v^*\frac{\partial \theta^*}{\partial y^*}) = \frac{\partial^2 \theta^*}{\partial x^{*2}} + \frac{\partial \theta^*}{\partial y^{*2}}, \tag{4.14}$$

where $Re = \frac{u_{ref}l}{\nu}$ and $Pr = \frac{\nu}{\alpha}$.

The nondimensionalized boundary conditions used in this problem are

$\theta^*(0,y^*,t^*)$=-45;

$u^*(8,y^*,t^*)$=0, $v^*(8,y^*,t^*)$=0, $\theta^*(8,y^*,t^*)$=10;

$u^*(x^*,0,t^*)$=0, $v^*(x^*,0,t^*)$=0, $\frac{\partial\theta^*}{\partial y^*}(x^*,0,t^*) = 0$;

$u^*(x^*,1,t^*)$=0, $v^*(x^*,1,t^*)$=0, $\frac{\partial\theta^*}{\partial y^*}(x^*,1,t^*) = 0$, and

liquid/solid interface conditions ($\partial\Omega_{ls}$).

The liquid/solid interface conditions, $\partial\Omega_{ls}$, use the following set of reference quantities to non-dimensionalize the governing equations at the solid/liquid interface

$$v_1{}^*=\frac{v_1}{u_{ref}},\ v_2{}^*=\frac{v_2}{u_{ref}},\ n^*=\frac{n}{L_{ref}},\ N^*=\frac{N}{L_{ref}},\ \theta^*=\frac{T\text{-}T_{ref}}{\Delta T},\ t^*=\frac{u_{ref}t}{L_{ref}}.$$

The conditions at the interphase then become

$$\rho_2\left(v_2{}^* - \frac{dN^*}{dt^*}\right) - \rho_1\left(v_1{}^* - \frac{dN^*}{dt^*}\right) = 0, \tag{4.15}$$

$$\rho_2\left(v_2{}^* - \frac{dN^*}{dt^*}\right) v_2{}^*{}_{(s)} - \rho_1\left(v_1{}^* - \frac{dN^*}{dt^*}\right) v_1{}^*{}_{(s)} = \tau_{1(s)} - \tau_{2(s)} + \frac{\partial\sigma}{\partial s}, \tag{4.16}$$

$$\rho_2\left(v_2{}^* - \frac{dN^*}{dt^*}\right) h_2 - \rho_1\left(v_1{}^* - \frac{dN^*}{dt^*}\right) h_1 = \frac{q_1\text{-}q_2}{u_{ref}}, \tag{4.17}$$

and for diffusional heat transfer in Fourier continua, the energy equation becomes

$$\alpha\ c\ \rho_1\ \frac{Pe}{Ja}\left(v_1{}^* - \frac{dN^*}{dt^*}\right) = -k_1\left(\frac{\partial\theta^*}{\partial n^*}\right)_s + k_2\left(\frac{\partial\theta^*}{\partial n^*}\right)_s, \tag{4.18}$$

where $Pe = \frac{U_{ref}L_{ref}}{\alpha}$ and $Ja = \frac{c\Delta T}{h}$.

An important non-dimensional quantity in this problem is the Grashof number, defined as

$$Gr = \frac{\beta g(\Delta T_{ref}) {L_{ref}}^3}{\nu^2},$$

where L_{ref} is the characteristic length, and in our case, it is the height of the cavity. For fixed T_f, latent heat of fusion, h, and other material properties and geometry, numerical calculations are carried out with Grashof numbers ranging from $3.55\text{x}10^{-3}$ to $1.065\text{x}10^{5}$. The Prandtl number in this case is set equal to 1, and Ja is 0.64.

Contour plots representing the isotherms, streamlines, and vorticity contours are shown in Figs. 4.12 to 4.17. These plots all show steady-state, time-independent results. As the Grashof number increases, the shape of the solid/liquid interface deforms. For small Gr, the interface appears straight. When Gr reaches 355, the interface starts to deform. Dragged by the flow, the interface deforms the most at the lower half, creating a counter-clockwise flow pattern. Up to a certain point, this interface does not move toward the cold side anymore, due to a melt back effect caused by T_h, the fixed above T_f temperature at the right side of the boundary. Numerical simulations for $Gr = 3.55\text{x}10^{-2}$, and 0.355 have also been conducted, but the results are not included, since they are not much different from the case of $Gr = 3.55\text{x}10^{-3}$.

For low Gr, the solidification front moves rather fast, while this speed slows down when Gr increases. A plot showing the propagation of the solidification front is shown in Fig. 4.18 for $Gr = 355$.

Fig. 4.19 is a *Log-Log* plot of dimensionless velocity, $|V^*|$ vs. Gr. We can see the the relationship between these two quantities starts with a linear one, and as Gr increases to the order of 355, the curve starts to bend. Eventually, the curve levels off. Due to computational difficulties, research on solutions for high

values of Grashof number was not conducted in this thesis.

A *Log-Log* plot of dimensionless streamfunction, ψ^* vs. Gr is shown in Fig. 4.20. This curve behaves in a similar way that the $|V^*|$ vs. Gr curve behaves. At low Gr numbers, there appears a linear relation between ψ^* and Gr. As Gr increases, the straight line starts to curve.

An analytical solution of problem S1 is carried out below to compare with the numerical solutions, Walker (1992). One restriction of this analytical solution is that it only applies to cases with undeformed solid/liquid interface. This implies small Gr numbers in our problem. From the previous diagrams, Figs. 4.12 to 4.17, we can see that as the Gr increases, the interface starts to deform and is no longer straight. For these large Gr cases, the analytical solution is not valid. Another limitation of this analytical solution is that it does not consider the motion in the liquid phase. The results do give the location of the solid/liquid interface and the temperature distribution within the the liquid or the solid phase.

Let's consider the following. We have an semi-infinite domain with solid and liquid interfacing each other. The solid/liquid interface propagates to the liquid region as time elapses (Fig. 4.21). The purpose of this problem involves finding the temperature distributions in both the solid phase and the liquid phase as functions of x.

First let's take a control element from the system. The energy balance on the element states that

$$E_i + E_g = E_o,$$

where E_i is the net energy going into the element, E_g is the net energy generated

within the element, and E_o is the net energy going out of the element. In another words

$$-k_s \frac{\partial T_s}{\partial x} + \rho h_{sf} \frac{\partial X}{\partial t} = -k_l \frac{\partial T_l}{\partial x},$$

where h_{sf} is the latent heat of fusion. As surface moves, $\rho h_{sf} dX$ is liberated and must be removed by conduction. Rearrange terms

$$k_s \frac{\partial T_s}{\partial x} - k_l \frac{\partial T_l}{\partial x} = \rho h_{sf} \frac{\partial X}{\partial t}, \tag{4.19}$$

and at the solid/liquid interface, i.e., at $x = X(t)$

$$T = T_s = T_l = T_f. \tag{4.20}$$

Now assume that the conduction is linear, and at the interface, $T_s(x,t) = T_f$. Therefore

$$\frac{\partial T_s}{\partial x} dx + \frac{\partial T_s}{\partial t} dt = 0,$$

and solving for $\frac{dx}{dt}$

$$\frac{dx}{dt} = -\left(\frac{\partial T_s}{\partial x}\right) / \left(\frac{\partial T_s}{\partial t}\right).$$

Plug $\frac{dx}{dt}$ into equation (4.19)

$$k_s \frac{\partial T_s}{\partial x} - k_l \frac{\partial T_l}{\partial x} = -\rho h_{sf} \left(\frac{\partial T_s}{\partial x}\right) / \left(\frac{\partial T_s}{\partial t}\right),$$

and for known T_l, equation (4.19) is nonlinear in T_s.

The governing equations can now be written as

$$\frac{\partial^2 T_s}{\partial x^2} = \frac{1}{\alpha_s} \frac{\partial T_s}{\partial t}, \tag{4.21}$$

for $x < X(t)$; and

$$\frac{\partial^2 T_l}{\partial x^2} = \frac{1}{\alpha_l} \frac{\partial T_l}{\partial t}, \tag{4.22}$$

for $x > X(t)$.

The boundary conditions in this case are

$$T_s \to T_{s0}, \text{ as } x \to -\infty,$$

$$T_l \to T_\infty, \text{ as } x \to \infty,$$

plus equations (4.19) and (4.20) at the moving interface.

The initial conditions involved in this problem are

$$T_l = T_\infty, \text{ at } x > 0;$$

$$T_s = T_0, \text{ at } x = 0, \text{ and for all } t.$$

An approximate solution can be found from these governing equations and the boundary conditions. First let's assume $T_l = T_f$, i.e., no temperature variation in the liquid phase. Then in the regions where $x < X(t)$

$$\frac{\partial^2 T_s}{\partial x^2} = \frac{1}{\alpha_s} \frac{\partial T}{\partial t}. \tag{4.23}$$

Assume $T_s = A + Bx$. At $x = 0$, $T_s = T_{s0}$. This gives $A = T_{s0}$. Similarly, at $x = X(t)$, $T_s = T_f$. And this gives $B = \frac{T_f - T_{s0}}{X(t)}$. Therefore

$$T_s = T_{s0} + (T_f - T_{s0}) \frac{x}{X(t)}.$$

The above equation satisfies equation (4.23) approximately if $\frac{X'}{X} << 1$.

This approximate solution can now be substituted into equation (4.19) and gives

$$\frac{k_s(T_f - T_{s0})}{X(t)} - 0 = \rho h_{sf} \frac{dX}{dt},$$

$$XdX = \frac{k_s(T_f - T_{s0})}{\rho h_{sf}} dt,$$

$$\frac{X^2 - X_0^2}{2} = \frac{k_s(T_f - T_{s0})t}{\rho h_{sf}},$$

and therefore

$$X(t) = (X_0^2 + \frac{2k_s(T_f - T_{s0})\, t}{\rho h_{sf}})^{1/2}.$$

The Neumann solution for a freezing liquid states that for $x > 0$, the liquid phase is at a temperature T_∞ - T_f. At $x = 0$, the temperature is at $T_0 < T_f$. For $x < X(t)$, $\frac{\partial^2 T_s}{\partial x^2} = \frac{1}{\alpha_s}\frac{\partial T_s}{\partial t}$ has a similarity solution in the form of

$$T_s(x, t) = A + B\ erf(\frac{x}{2(\alpha_s t)^{1/2}}).$$

In order to satisfy the condition at $x = 0$, A has to equal to T_0. And therefore

$$T_s(x, t) = T_0 + B\ erf(\frac{x}{2(\alpha_s t)^{1/2}}). \tag{4.24}$$

Similarly, for $x > X(t)$, $\frac{\partial^2 T_l}{\partial x^2} = \frac{1}{\alpha_l}\frac{\partial T_l}{\partial t}$ has a similarity solution in the following form

$$T_l(x, t) = C + D\ erfc\ (\frac{x}{2(\alpha_l t)^{1/2}}).$$

And as $x \to \infty$, $T_l \to T_\infty$. This gives $C = T_\infty$. Finally

$$T_l(x, t) = T_\infty + D\ erfc\ (\frac{x}{2(\alpha_l t)^{1/2}}). \tag{4.25}$$

Now let's go back to the interface of the solid and liquid phases. Apply equation (4.20) and obtain

$$T_0 + B\ erf(\frac{X(t)}{2\sqrt{\alpha_s t}}) = T_\infty + D\ erfc(\frac{X(t)}{2\sqrt{\alpha_l t}}) = T_f. \tag{4.26}$$

The above equation, equation (4.26) must be satisfied for all t. Hence

$$X(t) = 2\lambda\sqrt{\alpha_s t}, \tag{4.27}$$

where λ is a constant needs to be found. Equation (4.27) gives the location of

the solid/liquid interface as a function of time, t.

Employ boundary condition (1), it is easy to see that

$$k_s \frac{\partial T}{\partial x}|_{x=X(t)} = \frac{2B}{\sqrt{\pi}} k_s \frac{exp(-\frac{x^2}{4\alpha_s t})}{2\sqrt{\alpha_s t}}|_{x=X(t)} = \frac{Bk_s exp(-\lambda^2)}{\sqrt{\pi\alpha_s t}},$$

and

$$k_l \frac{\partial T}{\partial x}|_{x=X(t)} = -\frac{2D}{\sqrt{\pi}} k_l \frac{exp(-\frac{x^2}{4\alpha_l t})}{2\sqrt{\alpha_l t}}|_{x=X(t)} = -\frac{Dk_l exp(-\frac{\lambda^2\alpha_s}{\alpha_l})}{\sqrt{\pi\alpha_l t}}.$$

From equation (4.27), one can get

$$\rho h_{sf} \frac{\partial X}{\partial t} = \rho h_{sf} \frac{2\lambda}{2} (\frac{\alpha_s}{t})^{1/2} = \rho h_{sf} \lambda (\frac{\alpha_s}{t})^{1/2}.$$

Therefore the condition at the interface becomes

$$Bk_s exp(-\lambda^2) + Dk_l (\frac{\alpha_s}{\alpha_l})^{1/2} exp(-\lambda^2 \frac{\alpha_s}{\alpha_l}) = \rho\lambda h_{sf}\alpha_s\sqrt{\pi}. \tag{4.28}$$

From equation (4.26), one can easily obtain

$$B\ erf(\lambda) = T_f - T_0,$$

and

$$D\ erfc[\lambda (\frac{\alpha_s}{\alpha_l})^{1/2} = T_f - T_\infty.$$

And therefore, equation (4.28) becomes

$$\frac{exp(-\lambda^2)}{erf(\lambda)} + \frac{k_l}{k_s} (\frac{\alpha_s}{\alpha_l})^{1/2} \frac{exp(-\lambda^2 \frac{\alpha_s}{\alpha_l})}{erfc[\lambda(\frac{\alpha_s}{\alpha_l})^{1/2}]} \frac{(T_f - T_\infty)}{(T_f - T_0)} = \frac{\rho\lambda h_{sf}\alpha_s\sqrt{\pi}}{(T_f - T_0)k_s}.$$

Since $\frac{\alpha_s}{k_s} = \frac{1}{\rho} c_s$, thus

$$\frac{exp(-\lambda^2)}{erf(\lambda)} + \frac{k_l}{k_s} (\frac{\alpha_s}{\alpha_l})^{1/2} \frac{exp(-\lambda^2 \frac{\alpha_s}{\alpha_l})}{erfc[\lambda(\frac{\alpha_s}{\alpha_l})^{1/2}]} \frac{(T_f - T_\infty)}{(T_f - T_0)} = \frac{\lambda h_{sf}\sqrt{\pi}}{c_s(T_f - T_0)}. \tag{4.29}$$

Note here that the solution applies for the aforementioned initial conditions at X

$= 0$. Apply the initial conditions, and if $T_\infty = T_f$, then equation (4.29) simplifies to

$$\frac{exp(-\lambda^2)}{erf(\lambda)} = \frac{\lambda h_{sf}\sqrt{\pi}}{c_s(T_f - T_0)},$$

or

$$\lambda\, exp(\lambda^2)\, erf(\lambda) = \frac{c_s(T_f - T_0)}{h_{sf}\sqrt{\pi}}.$$

Finally, the temperature distributions in both the solid and the liquid phases are

$$T_s(x, t) = T_0 + \frac{T_f - T_0}{erf(\lambda)}\, erf(\frac{x}{2\sqrt{\alpha_s t}}), \tag{4.30}$$

and

$$T_l(x, t) = T_\infty + \frac{T_f - T_\infty}{erfc[\lambda(\frac{\alpha_s}{\alpha_l})^{1/2}]}\, erfc(\frac{x}{2\sqrt{\alpha_s t}}). \tag{4.31}$$

Substitute in the values of the parameters that are used in the numerical simulation, equations (4.30) and (4.31) become

$$T_s(x, t) = -45 + \frac{45}{erf(\lambda)} erf(\frac{x}{2\sqrt{t}}), \tag{4.30}$$

$$T_l(x, t) = 1 - \frac{erfc(\frac{x}{2\sqrt{t}})}{erfc(\lambda)}. \tag{4.31}$$

The two above equations give the temperature distribution in the solid as well as the liquid phase.

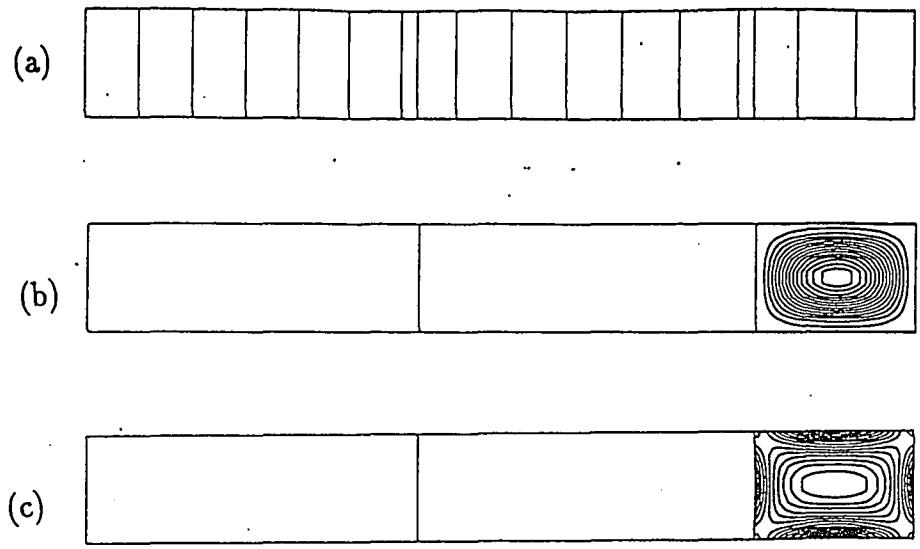

Fig. 4.12 Problem S1--Gr=3.55x10^{-3}.

(a) Isotherms, (b) Streamlines, (c) Vorticity contours.

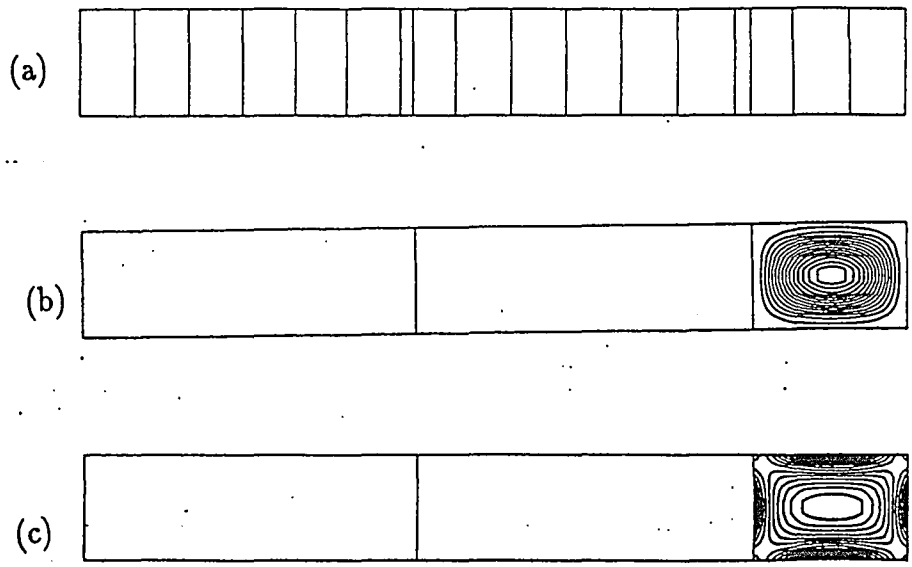

Fig. 4.13 Problem S1--Gr=35

(a) Isotherms, (b) Streamlines, (c) Vorticity contours.

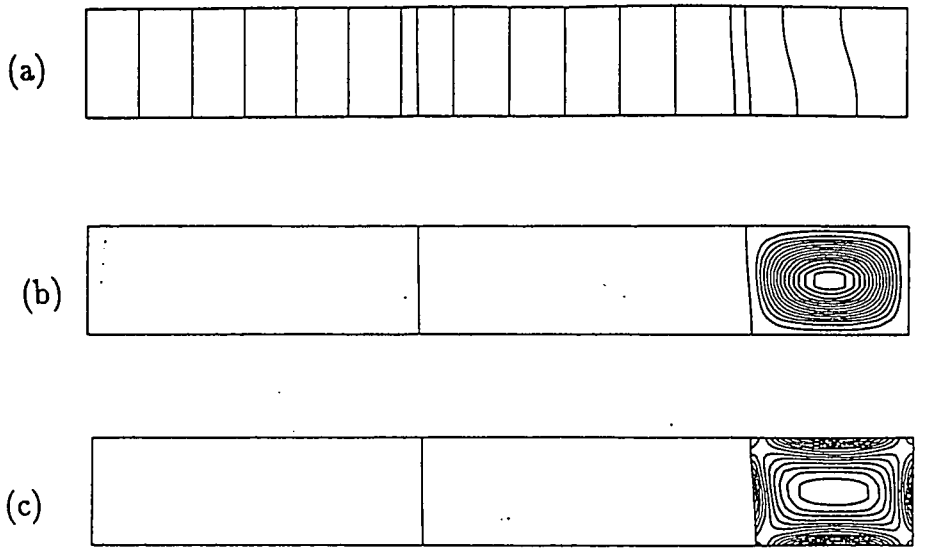

Fig. 4.14 Problem S1--Gr=355

(a) Isotherms, (b) Streamlines, (c) Vorticity contours.

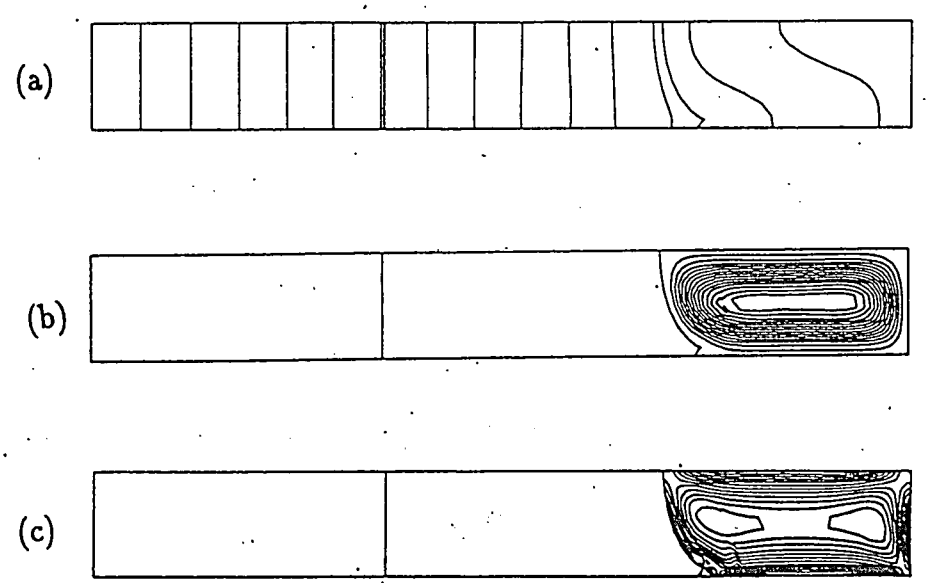

Fig. 4.15 Problem S1--Gr=3550

(a) Isotherms, (b) Streamlines, (c) Vorticity contours.

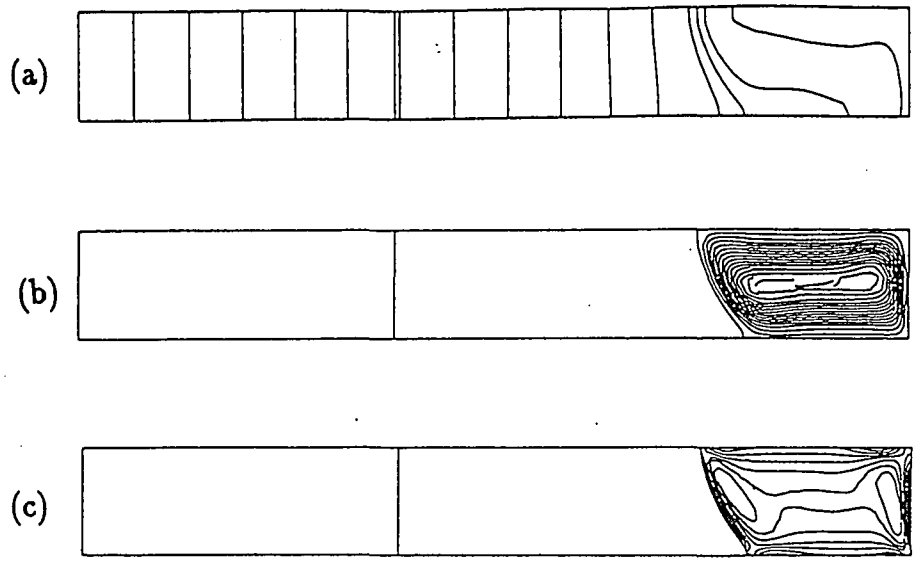

Fig. 4.16 Problem S1--Gr=35500

(a) Isotherms, (b) Streamlines, (c) Vorticity contours.

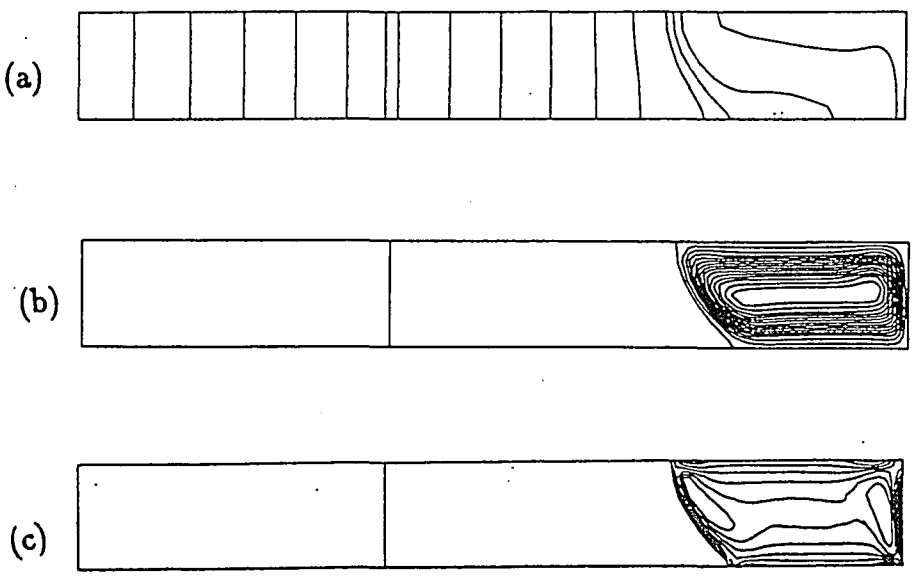

Fig. 4.17 Problem S1--Gr=106500

(a) Isotherms, (b) Streamlines, (c) Vorticity contours.

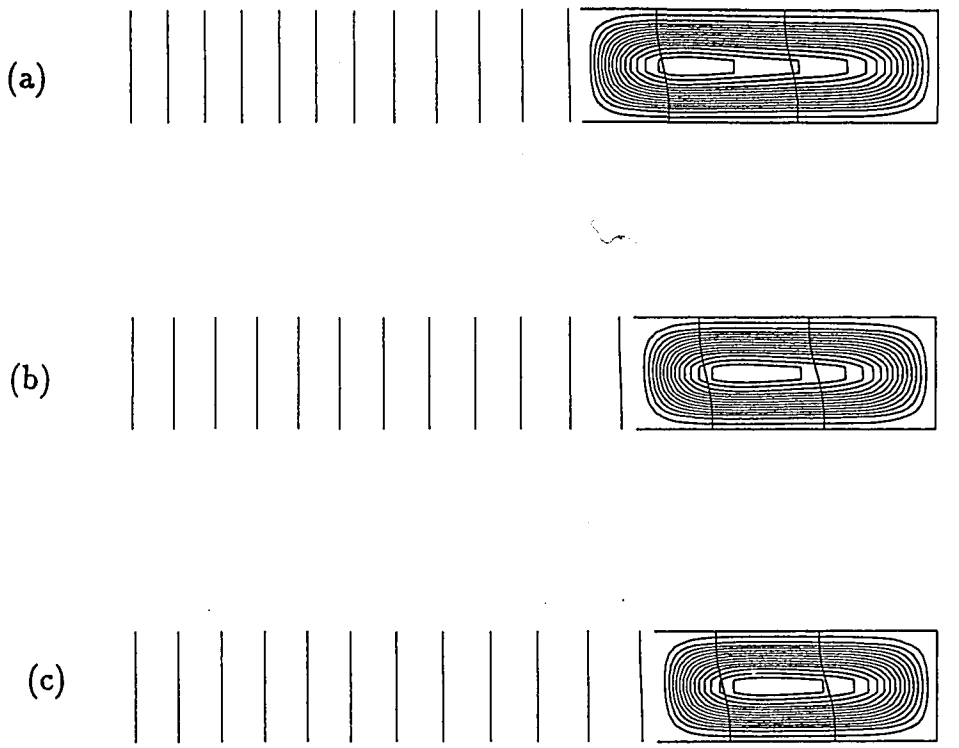

Fig. 4.18 Problem S1--Propagation of solidification front.
(a) t^*=15.6, (b) t^*=20.8, (c) t^*=22.8.

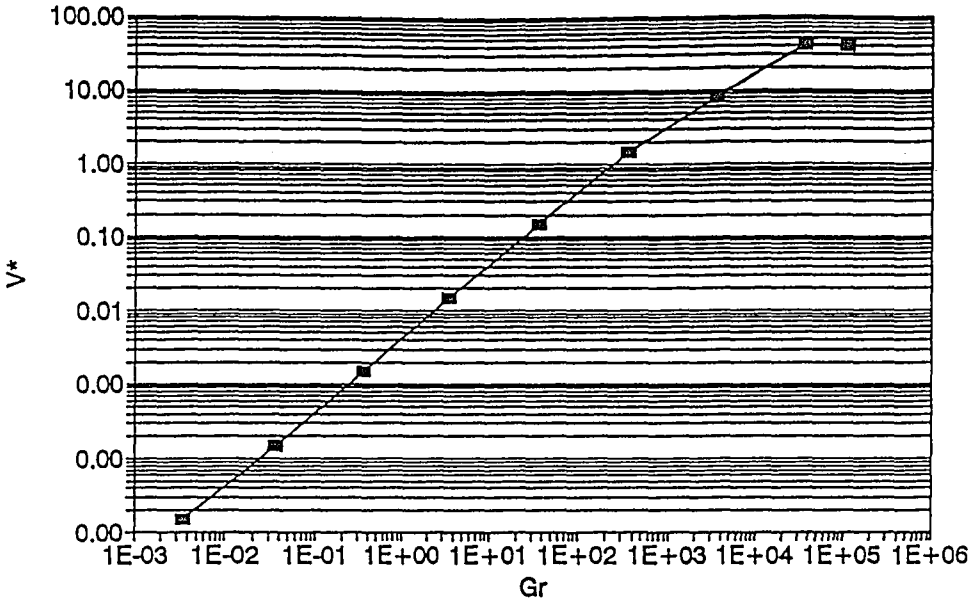

Fig. 4.19 Problem S1--$|V^*|$ vs. Gr

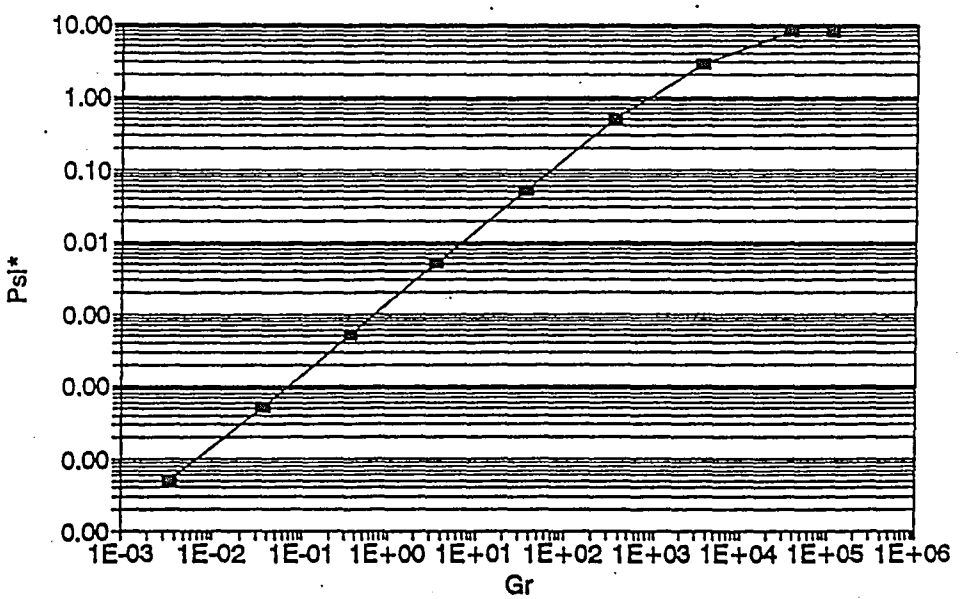

Fig. 4.20 Problem S1--ψ^* vs. Gr

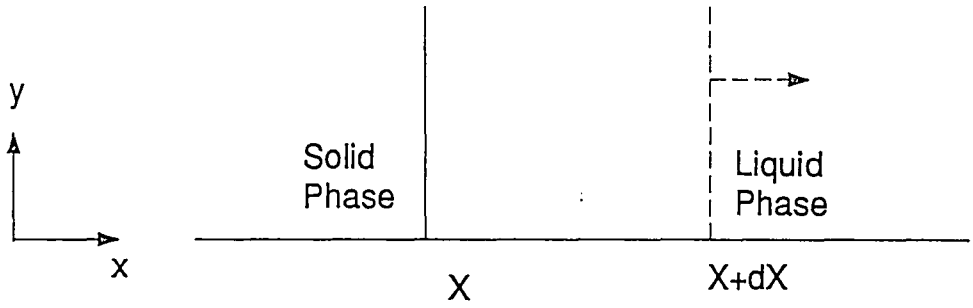

Fig. 4.21 Problem S1

(d) Problem TCS1

This problem is a combination of problem TC1 and problem S1. In this case, we are looking at the combined effect of thermocapillary convection and solidification. The geometry used here is a square cavity ($A = 1$) (Fig. 2.3 (d)).

The same set of reference quantities, as in problems TC1 and TC2 are used in this case again to non-dimensionalize the governing equations in the liquid phase

$$x^*=\frac{x}{L_{ref}},\ y^*=\frac{y}{L_{ref}},\ u^*=\frac{u}{u_{ref}},\ v^*=\frac{v}{u_{ref}},\ p^*=\frac{pL}{\mu u_{ref}},\ \theta^*=\frac{T\text{-}T_0}{\Delta T_{ref}},\ t^*=\frac{u_{ref}t}{L},$$

where $u_{ref} = \frac{-\frac{\partial\sigma}{\partial T}\Delta T}{\mu}$ and $\Delta T_{ref} = T_h - T_f$. The governing equations then become

$$\frac{\partial u^*}{\partial x^*} + \frac{\partial v^*}{\partial y^*} = 0, \tag{4.32}$$

$$Re\ (\frac{\partial u^*}{\partial t^*} + u^*\frac{\partial u^*}{\partial x^*} + v^*\frac{\partial u^*}{\partial y^*}) = -\frac{\partial p^*}{\partial x^*} + \frac{\partial^2 u^*}{\partial x^{*2}} + \frac{\partial^2 u^*}{\partial y^{*2}}, \tag{4.33}$$

$$Re\ (\frac{\partial v^*}{\partial t^*} + u^*\frac{\partial v^*}{\partial x^*} + v^*\frac{\partial v^*}{\partial y^*}) = -\frac{\partial p^*}{\partial y^*} + \frac{\partial^2 v^*}{\partial x^{*2}} + \frac{\partial^2 v^*}{\partial y^{*2}}, \tag{4.34}$$

$$Ma\ (\frac{\partial \theta^*}{\partial t^*} + u^*\frac{\partial \theta^*}{\partial x^*} + v^*\frac{\partial \theta^*}{\partial y^*}) = \frac{\partial^2 \theta^*}{\partial x^{*2}} + \frac{\partial \theta^*}{\partial y^{*2}}, \tag{4.35}$$

where $Re = \frac{\gamma \Delta T_{ref} L_{ref}}{\mu\nu}$ and $Pr = \frac{\nu}{\alpha}$.

The dimensionless boundary conditions are

$u^*(0,y^*,t^*)=0,\ v^*(0,y^*,t^*)=0,\ \theta^*(0,y^*,t^*)=1;$

$\theta^*(1.1,y^*,t^*)$=-15;

$u^*(x^*,0,t^*)$=0, $v^*(x^*,0,t^*)$=0, $\frac{\partial\theta^*}{\partial y^*}(x^*,0,t^*)$=0;

at y^*=1, free surface conditions ($\partial\Omega_{lg}$), equations (4.5) to (4.10) and liquid/solid interface conditions ($\partial\Omega_{ls}$), equations (4.15) to (4.18), located at x^*=1 at t^*=0.

In the process of numerically simulating this combined effects, we encountered many difficulties. We tried three different mesh designs in order to avoid numerical instability. Fig. 4.22 (a) shows the simplest mesh that was used. Instability occurred near the contact point of the free surface and the solid/liquid interface shortly after the beginning of the simulation. Then, a second design was brought out to resolve this problem (Fig. 4.22 (b)), but was not very successful. Lastly, we remeshed the corner using a "corner frame", as shown in Fig. 4.22 (c). This design was rather successful. Instability has not occurred since this latest mesh design was used, but the time step, Δt, was very small (in the order of 10^{-9} for dimensional computations). For such a small Δt, it would take an extremely long period of real computational time to pass the transient period. From the results that we have got so far, there has not been any deformation on the solid/liquid interface yet. Due to time limitations, we are not able to present the final steady-state solutions at this stage.

Plots of isotherms, streamlines, and vorticity contour patterns are presented in Fig. 4.23 to show a representative result during the transient process. Fig. 4.23 (a) shows that the greatest temperature gradient occurs within the solid phase. From Fig. 4.23 (b), we can see that the maximum

streamfunction is located close to the hot corner of the fluid region. A single vortex pattern also appears. The highest vorticity occur right below the free surface, at the cold corner of the region occupied by the liquid (Fig. 4.23 (c)). Due to low spatial resolution, the ω-contours are sometimes broken or wrinkled.

(a)

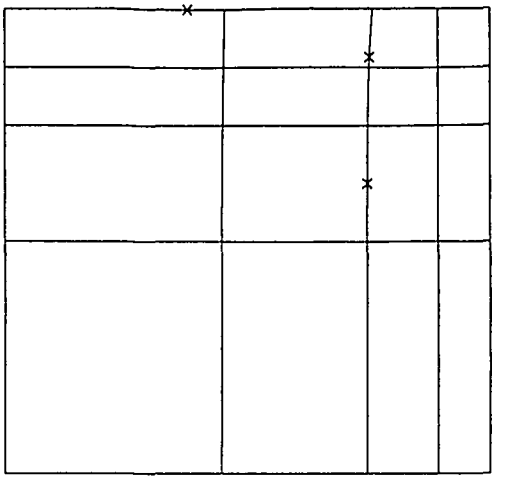

(b)

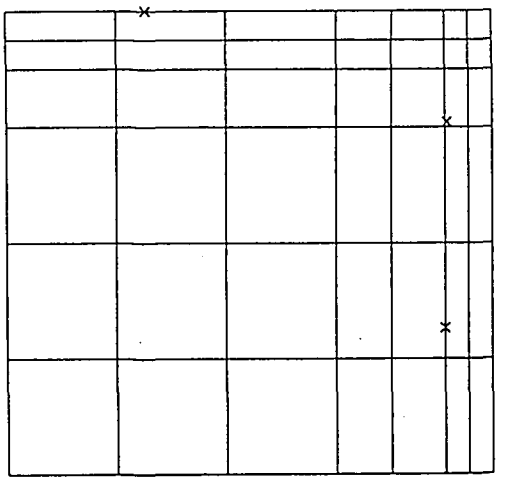

(c)

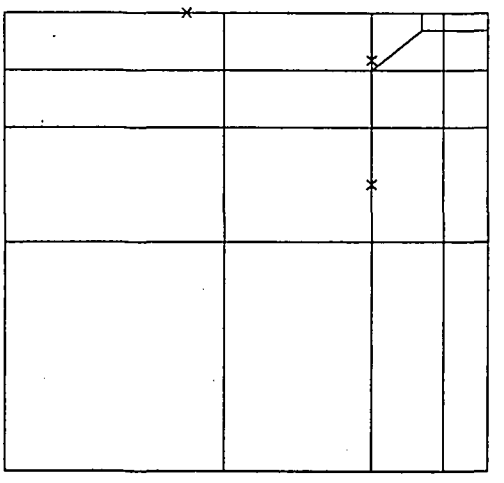

Fig. 4.22 Problem TCS1--Mesh Designs.

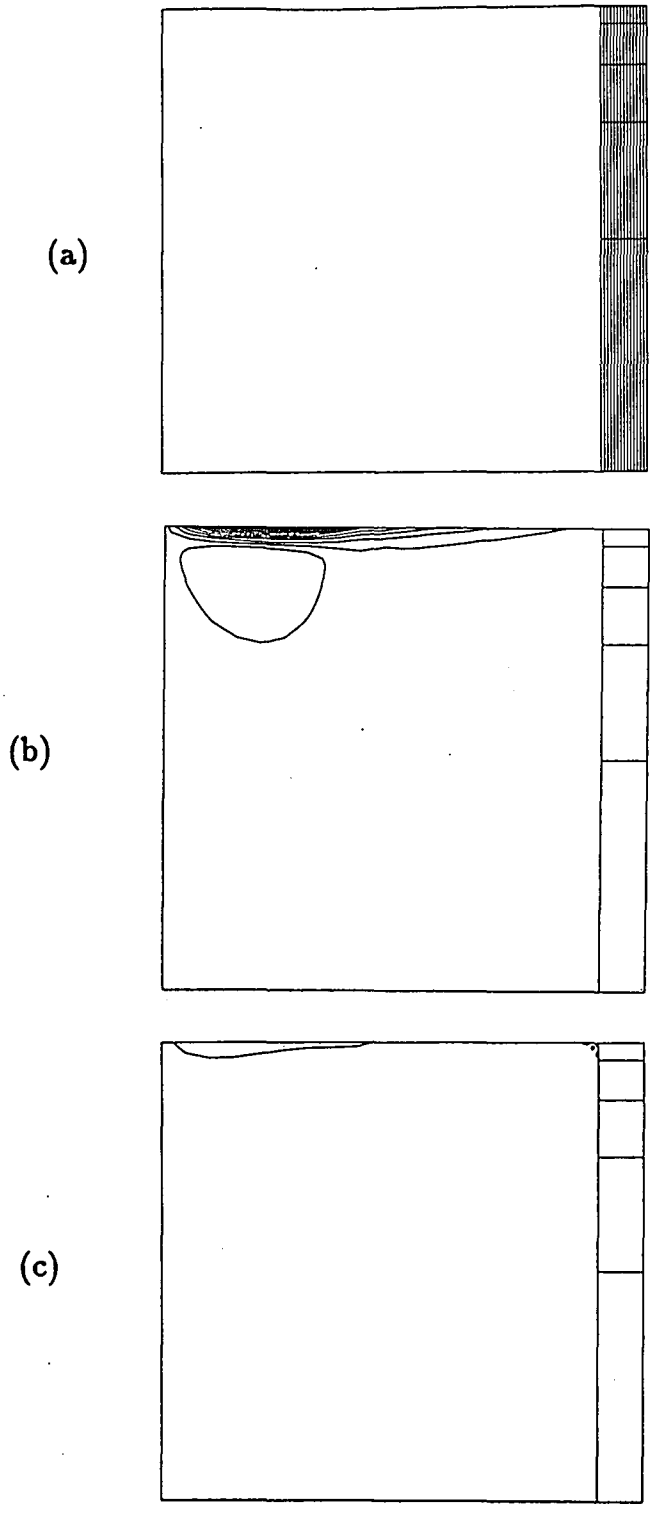

Fig. 4.23 Problem TCS1

(a) Isotherms, (b) Streamlines, (c) Vorticity contours.

V. CONCLUSIONS

The purpose of this thesis is to establish the feasibility of simulating accurately processes occurring during crystal growth from the melt using spectral element methods. Instead of trying to directly simulate the complex configurations encountered in practice, we have chosen to investigate four idealized problems that address the basic modeling issues to be resolved: thermocapillary convection, natural convection, and propagation of solidification fronts. All simulations performed are time accurate. If a steady (time-independent) solution exists it is found as the steady-state solutions of the appropriate initial boundary value problem after all transients die out, i.e., in the limit $t \to \infty$.

We have numerically simulated two different cases of thermocapillary convection processes, one case of solidification process in the presence of natural convection in the liquid phase, and one case of thermocapillary convection combined with phase change. For the three later cases, problems TC2, S1, and TCS1, we focused our attention to the fundamental steady-state properties. For the first case, problem TC1, we focused our attention to its transient characteristics.

The Π-groups for problem TC1 are: Re=7200, Pr=0.015, Ca=0.01, Bi=0, and Bo=0. Our focus in problem TC1 was to find a pattern of how the free surface deforms during the transient process and the associated streamline patterns. For the parameters considered here, a very long transient is observed, but the free surface oscillations eventually damp out.

The Π-groups for problem TC2 are: $10^2 \leq Re \leq 5\text{x}10^4$, Pr=0.01, Ca=0.01, and

Bo=0. Time-independent features, such as the isotherm, streamline, and vorticity patterns were studied for various Reynolds numbers. Free surface deformation, speed, and pressure distributions were also studied. Heat transfer characteristics were studied by investigating the relation between the average Nusselt number and the Reynolds number over the bottom wall. The relation is a weak one because of the small value of Pr. Solutions are time-independent and symmetric about the centerline of the computational domain. No temporal instabilities have been observed in the range of the parameters studied. As $Re \rightarrow \infty$, thin shear layers are formed close to the free surface and vorticity becomes constant in the regions of closed streamlines in accordance to the Prandtl-Batchelor theorem.

In problem S1 we studied a solidification process in a closed cavity with no thermocapillary effects, but with natural convection effects varied from negligible to strong. The reason for conducting this study was to later add the solidification effect to our existing thermocapillary flow problems and further investigate a more complicated combined case. The Π-groups in this case are: $3.55\text{x}10^{-3} \leq Gr \leq 1.065\text{x}10^{5}$, Pr=1, and Ja=0.64. Steady-state solutions were found for various Grashof numbers. A transient solution was investigated to show the characteristics of the propagation of the solidification front. Information on the behavior of maximum flow velocity and maximum streamfunction obtained in this work should be useful in scaling considerations for the problem at hand. An analytical solution was also carried out to check the numerical solutions. However, there are many limitations to the analytical solution. In contrast, numerical solutions can be obtained for a much wider

range of parameters.

The last problem, problem TCS1 is a combination of problems TC1 and S1. The Π-groups here are: Re=10^3, Pr=1, Gr=0, Bi=0, and Ja=0.014. In order to avoid computational instabilities and excessive mesh deformations, three different designs of the mesh are proposed, with the latest one ("corner-frame") being the most stable design. The real computing time required to simulate this problem was extremely high. A new numerical algorithm, allowing larger values of Δt, should be developed before attempting to simulate realistic configurations of crystal growth processes from the melt. Alternatively, a scaling of the problem can be devised in order to rigorously simplify the mathematical model.

REFERENCES

Ben Hadid, H., Roux, B., and Laure, P., 1989, "Thermocapillarity effects on the stability of buoyancy-driven flows in shallow cavities", *PCH PhysicoChemical Hydrodynamics*, Vol. 11, No. 5/6, pp 625-644.

Bergman, T. and Keller, J., 1988, "Combined buoyancy, surface tension flow in liquid metals", *Numerical Heat Transfer*, Vol. 13, pp 49-63.

Bergman, T. and Webb, B., 1990, "Simulation of pure metal melting with buoyancy and surface tension forces in the liquid phase", *Int. J. Heat Mass Transfer*, Vol. 33, No. 1, pp 139-149.

Buckle, U. and Peric, M., 1992, "Numerical simulation of buoyant and thermocapillary convection in a square cavity", *Numerical Heat Transfer, Part A*, Vol. 21, No. 2, pp 121-141.

Camel, D., Tison, P., and Favier, J., 1986, "Marangoni flow regimes in liquid metals", *Acta Astronautica*, Vol. 13, No. 11/12, pp 723-726.

Cardin, Ph., Nataf, H.-C., and Dewost, Ph., 1991, "Thermal coupling in layered convection: evidence for an interface viscosity control from mechanical experimental and marginal stability analysis", *J. Phys. II*, pp 599-622.

Carpenter, B. and Homsy, G., 1990, "High Marangoni number convection in a square cavity: Part II", *Phys. Fluids A*, Vol. 2, No. 2, pp 137-149.

Chen, J. and Kuan, S., 1992, "Thermocapillary convection in a rectangular cavity under the influence of surface contamination", *Int. J. Heat Mass Transfer*, Vol. 35, No. 11, pp 2905-2910.

Chen, J., Sheu, J., and Jwu, S., 1990, "Numerical computation of thermocapillary convection in a rectangular cavity", *Numerical Heat Transfer, Part A*, Vol. 17, pp 287-308.

Gadgili, A. and Gobin, D., 1984, "Analysis of two-dimensional melting in rectangular enclosures in presence of convection", *Transactions of the ASME*, Vol. 106, pp 20-26.

Lai, C. and Chang, C., 1991, "Two-dimensional thermocapillary flows with specified heat fluxes upon the free surface", *Journal of the Chinese Institute of Engineers*, Vol. 14, No. 3, pp 267-278.

Liu, A., Voth, T., and Bergman, T., 1993, "Pure material melting and solidification with liquid phase buoyancy and surface tension forces", *Int. Heat Mass Transfer*, Vol. 36, No. 2, pp 411-422.

Metzger, J. and Schwabe, D., 1988, "Coupled buoyant and thermocapillary convection", *PhysicoChemical Hydrodynamics*, Vol. 10, No. 3, pp 263-282.

Mundrane, M. and Zebib, A., 1993, "Two- and three-dimensional buoyant thermocapillary convection", *Phys. Fluids A*, Vol. 5, No. 4, pp 810-818.

Ostrach, S., 1982, "Low-gravity fluid flows", *Ann. Rev. Fluid Mech.*, 14: 313-345.

Ramaswamy, B. and Jue, T., 1992, "Analysis of thermocapillary and buoyancy-affected cavity flow using FEM", *Numerical Heat Transfer, Part A*, Vol. 22, pp 379-399.

Rivas, D., 1991, "High-Reynolds-number thermocapillary flows in shallow enclosures", *Phys. Fluids A*, Vol. 3, No. 2, pp 280-291.

Sen, A. and Davis, S., 1982, "Steady thermocapillary flows in two-dimensional slots", *J. Fluid Mech.*, Vol. 121, pp 163-186.

Schwabe, D., Moller, U., Schneider, J., and Scharmann, A., 1992, "Instabilities of shallow dynamic thermocapillary liquid layers", *Phys. Fluids A*, Vol. 4, No. 11, pp 2368-2381.

Shyy, W. and Chen, M., 1991, "Interaction of thermocapillary and natural convection flows during solidification: normal and reduced gravity conditions", *Journal of Crystal Growth*, Vol. 108, pp 247-261.

Walker, J., Advanced Heat and Mass Transfer class notes, 1993.

Young, G., McDonald, K., Palazoglu, A., and Ford, W., 1992, "Thermal modeling of Bridgman crystal growth using a boundary element approach", *Journal of Crystal Growth*, Vol. 118, pp 193-203.

Zebib, A., Homsy, G., and Meiburg, E., 1985, "High Marangoni number convection in a square cavity", *Phys. Fluids*, Vol. 28, No. 12, pp 3467-3476.

Vita

Xun L. Chen was born in Shanghai, China on June 3, 1970 to Ming-San and Nai-Yu Chen.

She graduated from University of Maryland at College Park with a Bachelor of Science in Mechanical Engineering in August 1992 with high honors. She is a member of the Tau Beta Pi and the Pi Tau Sigma Honor Societies.

She began her graduate studies in Mechanical Engineering at Lehigh University in September 1992.

END

OF

TITLE